UNIVERSIDAD EAFIT

Cultivable Microbial Community Structure Along a Light Gradient in a Tropical Volcaniclastic Cave

Bachelor's Thesis

Submitted to the Area of Natural Systems and Sustainability
in Partial Fulfillment of the Requirements for the Degree of
Bachelor of Science in Biology

BY

Sebastian Correa-Gallego

ADVISOR

Dr. Nicolás Pinel Peláez

Medellín, Colombia

May 2026

This thesis is the result of a slow but persistent research process that began in 2022 with the exploration of ideas and literature on cave ecology, microbial life, and extremophilic systems. Over time, these early interests were refined into a defined scientific question, an experimental framework, and an integrated study of microbial diversity in Organal San Antonio. I conducted the field and laboratory activities, data analysis, interpretation, and manuscript preparation mainly during 2025 and 2026 at Universidad EAFIT.

All scientific content—including the research question, experimental design, field and laboratory execution, data analysis, interpretation, and final conclusions—is the author's own work and has not been submitted for any other degree. During the manuscript review and formatting stages, the author used Claude (Anthropic PBC, San Francisco; models Sonnet 4.5 and Sonnet 4.6) as a computational assistant for statistical code review, English prose refinement, and document formatting. The tool was used under direct author instruction and critical supervision. No scientific, analytical, or interpretive decision was delegated to artificial intelligence, and the author bears sole responsibility for the content, accuracy, and conclusions of this thesis.

Abstract

Cave environments compress sharp changes in light, energy input, surface connectivity, and substrate heterogeneity into short spatial gradients. This makes them powerful natural systems for examining microbial responses to environmental heterogeneity. Yet the cultivable microbial fraction of tropical volcaniclastic caves remains poorly resolved. Organal-type pseudokarstic caves of the Colombian Andes are especially underrepresented in cave microbiology, despite their distinctive geomorphology and hydrological connection to montane landscapes. Here, I tested whether sector identity along the light-defined zonation of the Organal San Antonio, a tropical volcaniclastic cave at ~2350 m a.s.l. in Támesis, Antioquia, is associated with differences in the R2A-recoverable microbial fraction of cave sediments. Two cultivation experiments were conducted: an initial binary Light–Dark comparison and a primary three-sector experiment resolving Entrance, Transition, and Dark zones with aliquot-level gravimetric normalization, 15 °C incubation, and a twenty-three-cluster operational phenotypic crosswalk. In the primary experiment, cultivable density followed a step-like pattern across the gradient: Entrance and Transition sediments supported approximately 5.1–5.6 $\times 10^5$ CFU g^{-1} field-moist sediment, whereas the fully aphotic Dark sector supported approximately 8.9×10^4 CFU g^{-1}, a roughly sixfold reduction ($\eta^2 = 0.652$). Local morphotype-cluster richness and evenness showed no detectable sector-level differences, but community composition partitioned strongly with zonation (PERMANOVA $R^2 = 0.573$, $p = 0.001$) under balanced multivariate dispersion. The Transition sector supported a distinctive set of zone-restricted phenotypic clusters, contributing approximately 27% of its cultivable community, while the Dark sector combined reduced density with moderate abundance of aphotic-restricted clusters. Preliminary Gram, KOH, catalase, and microscopic characterization of representative isolates revealed Gram-level uncertainty and cellular heterogeneity within several cross-sector colony phenotypes, confirming that the morphotype crosswalk is useful for community-level comparison but not equivalent to taxonomic resolution. These results establish a first spatially resolved cultivable baseline for an organal-type tropical volcaniclastic cave and indicate that sector identity along a light-defined cave gradient is associated with lower cultivable density in the aphotic sector and strong morphotype-level compositional turnover, without a parallel decline in local morphotype-cluster diversity. The study defines the scale at which these patterns are valid: the aerobic, low-temperature, dilute-R2A cultivable fraction of sediment-associated microorganisms.

Keywords: cave microbiology, cultivable fraction, volcaniclastic cave, morphotype crosswalk, environmental filtering, tropical Andes

Acknowledgments

This work grew from an interest in how microbial communities are organized under environmental constraint — an interest that, over the course of this research process, was sharpened by the discipline of careful observation and the demands of rigorous experimental design. The cave provided a tractable system; the questions it opened are considerably larger than the system itself.

I am deeply grateful to the municipality of Támesis and to the community surrounding Organal San Antonio, and especially to Rodrigo Echeverri, for opening their territory to this research and for sharing ecological, historical, and local knowledge that no textbook could have provided.

Nicolás Pinel guided this project from its earliest formulation to its final form. His influence on the way I structure questions, evaluate evidence, and demand precision from myself extends well beyond this manuscript. He taught me that rigor and genuine curiosity are not in tension.

I am also grateful to Dr. Valeska Villegas-Escobar for her critical perspective and institutional support throughout this work.

I thank Dr. Sergio Muñoz-Gómez for hosting me as a visiting undergraduate student at Purdue University during a period that profoundly shaped the way I think about biology and evolution. At Purdue, I found a scientific and human community built with integrity, generosity, and intellectual seriousness. Many people there became part of what I am now and of what I hope to become in life and in science.

The Fundación Fraternidad Medellín made my undergraduate education possible, including my visiting period at Purdue University. Nicolás Pinel secured essential field and logistical resources for the sampling campaigns. Universidad EAFIT provided the institutional space for the experimental work and a collaborative environment that supported many stages of this process.

I also thank my parents and my closest family for what no institution can provide: a sustained commitment to a process whose outcome was never guaranteed. Their support remained present through the most demanding moments of this path.

I hope to continue pursuing questions at the intersection of microbial ecology, physiology, and evolution.

Contents

1 Introduction

1.1 Caves as energy-limited habitats and environmental filters

The organization of life along environmental gradients is among the oldest and most productive observations in biology [1, 2]. From the treeline on a mountainside to the oxygen minimum zone of a stratified ocean, the spatial arrangement of organisms reflects the intersection of physiological tolerance with the physical structure of the environment. Wherever an abiotic variable changes predictably across space, communities respond: density shifts, composition turns over, and the functional repertoire of the assemblage reorganizes to match what local conditions will sustain. Subterranean environments offer a well-suited natural setting in which to study this relationship, because they compress steep environmental change into short spatial distances and maintain it with a temporal stability that few surface systems can match.

Caves impose a distinctive combination of constraints on biological communities: the progressive elimination of photosynthetically active radiation with depth, chronic nutrient scarcity, restricted atmospheric exchange, thermal buffering relative to surface conditions, and persistently high relative humidity [3–6]. These conditions act as abiotic filters whose intensity changes predictably along the entrance-to-interior gradient, selecting for organisms capable of sustaining metabolic activity under chronic stress and generating spatial gradients along which microbial communities are expected to change in density, composition, and functional organization.

Despite these constraints, caves harbor microbial communities of considerable diversity. Direct cell counts from rock surfaces and sediments routinely yield densities on the order of 10^6 cells per gram [5, 7], and molecular surveys have shown that subterranean assemblages include representatives of most major bacterial phyla. Across geographically and geologically diverse systems, using current prokaryotic phylum nomenclature [8], Pseudomonadota (Proteobacteria), Actinomycetota, Bacillota, and Chloroflexota are consistently among the most abundant lineages, with additional contributions from Acidobacteriota, Planctomycetota, Nitrospirota, and members of the candidate phyla radiation [5, 9–11]. This taxonomic breadth is maintained under extreme oligotrophy: dissolved organic carbon concentrations in cave waters are typically below 2 mg/L [7], and the primary sources of carbon and energy are limited to allochthonous inputs via percolating water, airborne deposition, root penetration, and invertebrate activity, supplemented in some systems by autochthonous chemolithoautotrophic production [6, 12, 13].

The persistence of life under such constraint reflects physiological adaptations operating at scales far below those captured by standard laboratory cultivation. In the deep subsurface, microorganisms catabolize 10^4- to 10^6-fold more slowly than model organisms in nutrient-rich cultures, turn over their biomass on timescales of centuries to millennia, and subsist with energy fluxes a thousand-fold below laboratory maintenance estimates [14]. Hoehler and Jørgensen formalized the concept of basal maintenance power — the minimum energy requirement for non-growing organisms to preserve cellular integrity — and showed that mean cell-specific metabolic rates in subsurface communities scatter several orders of magnitude below the rates required for

laboratory cultivation. Lever and colleagues subsequently distinguished three physiological states — growth, maintenance, and survival — that define the continuum of metabolic activity under increasing energy scarcity [15]. Cave environments are not as energy-depleted as the deep subsurface, but they share the fundamental characteristic of persistent carbon and energy limitation that selects for organisms with high substrate affinity, low basal metabolic rates, and efficient biosynthetic regulation [6, 7].

The internal structure of caves is commonly described through a three-zone model based on light penetration (Figure 1): an entrance zone that receives direct or indirect sunlight and is influenced by surface microclimate; a twilight zone where irradiance is strongly attenuated but not entirely absent; and a dark zone where light is undetectable and environmental parameters remain thermally and hydrologically stable over time [16–18]. Each zone imposes distinct selective pressures and supports different microbial functional types. In entrance zones, phototrophic microorganisms — particularly Cyanobacteria and green algae — colonize moist rock surfaces and form pigmented surface-associated communities sustained by residual irradiance; in carbonate cave systems, such assemblages have been shown to contribute to litholysis through acid secretion and to lithogenesis through biocalcification and the formation of structured surface coatings [18, 19]. Within the twilight zone, where irradiance can fall to less than 0.01% of surface levels within a few meters of the entrance, photosynthetically supported communities give way to heterotrophic assemblages dependent on allochthonous organic matter transported by dripwater, root exudates, or invertebrate vectors [5, 6]. In the fully aphotic interior, microbial life depends on chemolithoautotrophy — exploiting reduced iron, manganese, sulfur, or nitrogen compounds as energy sources — on the recycling of endogenous organic matter within microbial consortia, or on the slow degradation of mineral-associated carbon [3, 15, 20]. Beyond carbon cycling, caves host complete biogeochemical networks that operate independently of surface productivity: nitrogen cycling processes, including ammonia oxidation and biological nitrogen fixation, have been documented in lava cave microbial mats through detection of *amoA* and *nifH* marker genes [20, 21], and sulfur cycling, manganese and iron oxidation, and methane consumption have all been demonstrated in subterranean communities [3, 20].

These energetic and structural constraints intersect with the ecological concept of environmental filtering — the process by which abiotic conditions prevent the establishment or persistence of species that cannot tolerate local stressors [22]. The term is sometimes invoked loosely in the ecological literature, but caves provide a clear conceptual setting for its application: darkness, oligotrophy, low temperature, high humidity, and restricted exchange with the surface can act as filters whose intensity changes over short spatial distances. The resulting community structure is therefore expected to reflect the differential persistence, growth, or detectability of organisms able to meet the energetic and physiological demands of each sector, producing spatial turnover in density and composition. Empirical support for this view comes from the California lava cave study of Lavoie and colleagues, in which only 11.2% of operational taxonomic units were shared between cave microbial mats and overlying surface soils, and the number of cave entrances — a proxy for connectivity with the surface — was a significant predictor of community diversity

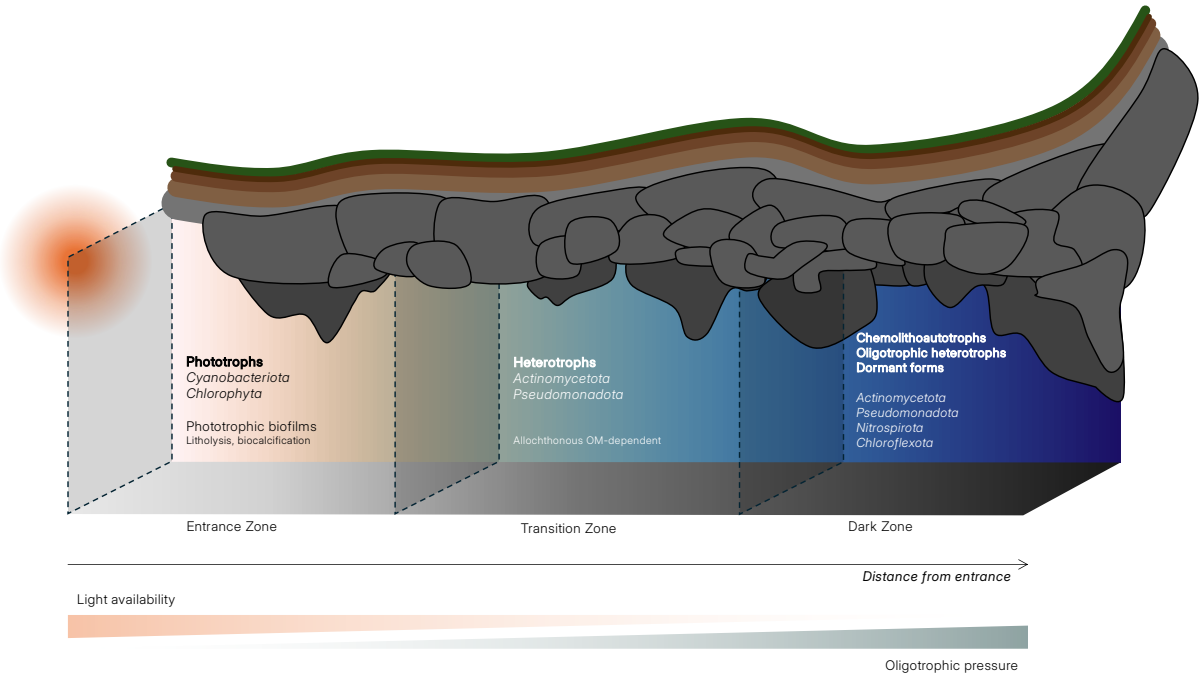

Figure 1. Conceptual model of light-defined cave zonation. The schematic represents the transition from a semi-illuminated entrance zone to a twilight transition sector and a fully aphotic dark zone, with decreasing light availability and stronger oligotrophic constraints toward the interior. Biological groups and ecological processes shown within the figure summarize theoretical expectations from cave microbiology and geomicrobiology; they are not taxonomic assignments or functional measurements from the present study. Taxonomic names refer to groups commonly reported in cave-associated microbial literature, whereas functional labels indicate broad ecological strategies expected along subterranean energy gradients. The cultivation-based analyses in this manuscript evaluated cultivable density, local morphotype-cluster diversity, and compositional turnover among sectors.

[23]. A recent global-scale meta-analysis of over 1,050 bacterial and fungal communities from caves worldwide further demonstrated that outdoor climate, particularly temperature and precipitation, is a primary driver of cave microbial diversity at regional and continental scales, selecting for specific dominant taxa across biogeographic boundaries [24]. Together, these lines of evidence indicate that subterranean communities are not random assemblages but spatially organized systems whose composition can respond to environmental gradients, structured by the interplay between external climate, internal abiotic constraints, and surface connectivity.

1.2 The karstic bias and the volcaniclastic gap

The geographic and geological scope of subterranean microbial ecology research is markedly uneven. The large majority of studies have been conducted in karstic limestone caves at temperate latitudes [4, 24, 25]. Karstic systems form through the dissolution of carbonate rocks by percolating acidic water, producing extensive drainage networks, chemically buffered substrates, and relatively continuous inputs of dissolved organic matter from overlying soils. Carbonate dissolution provides a steady supply of calcium, magnesium, and bicarbonate ions that buffer pH and sustain diverse mineral precipitations [3, 9]. Karst landscapes comprise approximately 15–20% of Earth's ice-free land surface [9], and their accessibility, speleothem-rich interiors, and hydrological connectivity with surface water systems have made them the default

model for subterranean microbiology. The microbial communities documented in karstic caves — including diverse assemblages of lithoautotrophs, denitrifiers, sulfur and iron oxidizers, and heterotrophic taxa — reflect these relatively favorable geochemical conditions and have provided the empirical foundation for most current understanding of cave microbial ecology [3, 5, 26].

Volcanic and volcaniclastic caves constitute a structurally and geochemically distinct category that remains comparatively undercharacterized [10]. These systems form through fundamentally different speleogenetic processes: lava flow dynamics produce lava tubes, in which the outer crust of a flowing lava stream solidifies while molten material continues to drain beneath; gravitational collapse of volcanic deposits produces talus and boulder caves; and the long-term erosive reconfiguration of pyroclastic materials produces volcaniclastic cavities of variable geometry [27, 28]. Unlike karstic caves, volcanic and volcaniclastic caves are typically geologically younger, chemically less buffered, and hydrologically less connected to surface water inputs. Their substrates — basaltic lavas, breccias, agglomerates, or reworked ignimbrites — offer different mineral compositions, surface textures, and trace-element availabilities than carbonate rocks. Basaltic substrates may provide reduced iron, manganese, and sulfur compounds that support chemolithotrophic metabolism, but the absence of continuous carbonate dissolution reduces allochthonous nutrient input, imposing more severe and persistent oligotrophy than is typical of karstic systems [27, 29].

Microbial ecology research in volcanic caves has been concentrated almost exclusively in lava tubes from a limited number of geographic regions: Hawaii, the Azores, the Canary Islands, New Mexico, California, and Sicily. The earliest molecular characterizations by Northup and colleagues across Hawaiian and Azorean lava caves identified at least fifteen bacterial phyla in microbial mats and secondary mineral deposits, with Actinobacteria, Acidobacteria, and Proteobacteria emerging as dominant lineages and geographic location proving a stronger determinant of community composition than local substrate characteristics [27, 30]. Hathaway and colleagues subsequently demonstrated that lava cave communities support functionally complete nitrogen cycles, with *Nitrosospira*-like ammonia-oxidizing bacteria dominant in Azorean caves and surface land use influencing the nitrogen-cycling communities below [21]. Riquelme and colleagues documented prominent Actinobacteria across fourteen volcanic caves on two Azorean islands, finding that cave identity and island location were more important than mat color in structuring microbial diversity [31]. A landmark comparison of seven California lava cave communities with overlying surface soils by Lavoie and colleagues revealed that only 11.2% of operational taxonomic units were shared between cave mats and soils [23], overturning the assumption that cave microorganisms are simple subsets of surface communities and providing strong evidence for indigenous, locally adapted assemblages shaped by *in situ* environmental filtering rather than passive deposition.

More recent work has continued to expand the geographic and ecological scope of volcanic cave microbiology. Nicolosi and colleagues conducted the first systematic study of Mount Etna lava tubes, finding communities dominated by Actinomycetota — particularly the genus *Crossiella* — together with Pseudomonadota, Acidobacteriota, and Chloroflexota [32]. Prescott and

colleagues compared Hawaiian lava caves of different geological ages and identified Chloroflexi as ecological hub species maintaining disproportionately many co-occurrence interactions within cave microbial networks [33]. Gonzalez-Pimentel and colleagues documented the involvement of prokaryotic communities in major element biogeochemical cycles within a Canary Islands lava tube, demonstrating active iron and manganese cycling on basaltic surfaces [34]. A comparative review across limestone, sulfuric acid speleogenetic, and volcanic caves found that limestone and lava tube caves are colonized by largely overlapping phyla — dominated by Pseudomonadota and Actinomycetota — while sulfidic caves show characteristic co-dominance of Pseudomonadota and Campylobacterota driven by chemolithoautotrophic sulfur oxidation [10].

Despite this growing body of work, published volcanic cave microbiology has been concentrated overwhelmingly in lava tubes — a specific speleogenetic type characterized by relatively smooth basaltic walls, broadly cylindrical geometry, and formation through active lava flow dynamics. Volcaniclastic caves, formed through the weathering, gravitational collapse, and erosive reconfiguration of pyroclastic deposits, represent a geologically and structurally distinct category with different substrate compositions, porosity regimes, and hydrological connectivities [28, 35]. The pyroclastic origin of these systems implies a heterogeneous distribution of mineral grains, variable permeability, and a more complex internal architecture than is typical of lava tubes, with implications for both the physical microhabitats available to microbial colonizers and the geochemical environment they encounter. Whether the ecological patterns documented in lava tube microbiology — zonation-associated community turnover, the dominance of Actinomycetota and Pseudomonadota, indigenous rather than surface-derived communities — generalize to volcaniclastic settings, or whether the geological and geochemical differences impose distinct selective pressures on microbial community structure, remains largely unresolved. This gap is particularly acute for tropical montane regions, where stable low temperatures, high humidity, mineral heterogeneity, and steep light-defined zonation may create selective landscapes with no direct analog in the existing literature. To my knowledge, no published study has examined cultivable microbial community structure in an organal-type tropical volcaniclastic cave, nor has any investigation addressed the pseudokarstic boulder caves characteristic of the Colombian Andes from a microbiological perspective.

1.3 Cultivation as a complementary approach

The great plate count anomaly — the one-to-four-orders-of-magnitude discrepancy between direct microscopic counts and colony counts on standard media — has been recognized since the 1980s as a fundamental limitation of culture-dependent microbiology [36]. In oligotrophic cave environments, culturability may be as low as 0.02–1% of total cell counts [37, 38]. Molecular methods now dominate the field, and their contributions to mapping subterranean microbial diversity are substantial [5, 39]. However, molecular and culture-based approaches capture fundamentally different dimensions of microbial communities and are best understood as complementary [40]: DNA-based methods cannot distinguish viable organisms from environmental DNA derived from dead or dormant cells, whereas cultivation enables the recovery of

living organisms, quantitative estimation of cultivable density through colony-forming unit counts, and phenotype-resolved community descriptions through morphotype classification [37, 41]. Cultivation also accesses members of the rare biosphere that fall below molecular detection limits — Shade and colleagues showed that cultivation can recover bacterial OTUs that are rare or undetected in culture-independent surveys, demonstrating that culture-dependent and sequencing-based approaches access overlapping but non-identical fractions of microbial diversity [42].

Low-nutrient media such as R2A agar, developed by Reasoner and Geldreich for the recovery of heterotrophic bacteria from potable water [41], are designed to overcome the nutrient shock that rich media impose on oligotrophic organisms. R2A has become the *de facto* standard for environmental heterotrophic plate counts and is widely used in cave microbiology, often at one-quarter or one-tenth strength to favor the recovery of organisms adapted to extreme oligotrophy. When combined with cave-mimetic incubation conditions — low temperature, darkness, and extended incubation periods — dilute R2A provides an ecologically relevant framework for recovering slow-growing phenotypes that would be missed by standard cultivation protocols. Kato and colleagues showed that colonies emerging after seven or more days on low-nutrient media can include phylogenetically novel bacteria, including taxa representing entirely new taxonomic orders [43]. In cave systems, Zhu and colleagues used intensive cultivation to recover 3,562 bacterial isolates representing 329 species, including fourteen newly described species, from rock, water, and sediment samples collected in two Chinese karst caves; they then integrated this cultivated genome collection with metagenomic data to infer metabolic potential in carbon, nitrogen, and sulfur cycling [26].

Despite this potential, spatially resolved cultivable baselines for cave systems remain scarce. Most culture-based cave studies report either bulk CFU counts without spatial replication or taxonomic identifications of selected isolates without community-level statistical analysis [23, 44]. Colony morphotyping — the systematic classification of colony-level phenotypes including pigmentation, shape, elevation, margin architecture, size, surface texture, transparency, spreading behavior, and mucoidity — provides a practical framework for resolving community composition at the plate level when molecular identification of every isolate is not feasible. The defensibility of morphotyping as a community-ecology tool rests on empirical validation: Haldeman and Amy, working with deep subsurface rock isolates, used fatty acid methyl ester chemotaxonomic profiling to show that isolates within a single morphotype generally corresponded to the same species at the biotype or subspecies level [45]; Lebaron and colleagues, working with seawater bacteria, used 16S rRNA gene restriction analysis to demonstrate that different colony morphotypes generally corresponded to different species, while noting that morphotyping inevitably underestimates true taxonomic diversity because morphological convergence can obscure phylogenetic differences [46]. Morphotyping therefore captures a coarse but meaningful resolution of colony-level community structure, sufficient for detecting spatial patterns of compositional change while remaining explicitly non-taxonomic. To my knowledge, no prior

study has applied multivariate ecological statistics to morphotype-level cultivable community data from an organal-type volcaniclastic cave system.

1.4 The study system: the Organal San Antonio

The Organal San Antonio is a tropical volcaniclastic cave located at approximately 2350 m a.s.l. in the municipality of Támesis (Antioquia), on the eastern flank of the Western Cordillera of the Colombian Andes (Figure 2). The cave belongs to a distinctly Antioquian category of pseudokarstic systems known as *organales*, first systematically classified in the geological literature by Cano Alzate and Rentería Cárdenas, who proposed a formal typology based on lithology, speleogenetic process, hydrological regime, and structural stability [47]. Organales are subterranean passages formed by the gravitational accumulation and long-term reorganization of large volcanic boulders, producing cave-like corridors that occasionally channel running water. They lack internal speleothems and have no dissolution-based speleogenesis; their formation is therefore interpreted as predominantly mechanical and erosive, reflecting the gravitational reorganization of volcaniclastic materials over geological timescales. Within the Cano Alzate & Rentería Cárdenas typology, the Organal San Antonio is classified as a humid, deep, large, stable, gravitational, igneous-volcanic, supported, and semiconfined system — generated not by dissolution of soluble rock, but by gravitational accumulation, mechanical reorganization, and erosive modification of a heterogeneous volcaniclastic substrate. Consistent with this interpretation, the system is best treated as pseudokarst rather than karst: its voids are produced by mechanical accumulation, gravitational reorganization, and erosive modification of volcaniclastic materials, not by dissolution of soluble bedrock. This places organales within the broader family of non-dissolution subterranean forms comparable to talus caves, boulder caves, and related pseudokarstic cavities described worldwide [28, 35, 47].

The geological context of the Organal San Antonio is provided by the Combia Volcanic Province, a Miocene volcanic unit active between approximately 12 and 6 Ma within the Cauca–Romeral fault system of the Western Cordillera [48, 49]. The Combia Province encompasses three coexisting magmatic series — tholeiitic, calc-alkaline, and shoshonitic — and includes a heterogeneous assemblage of basaltic lavas, andesites, pyroclastic deposits, debris-avalanche and lahar deposits, and subvolcanic porphyritic bodies emplaced during the late Miocene. Its formation has been linked to the subduction of the Nazca plate beneath the South American plate and to the collision of the Panamá-Chocó block with northwestern South America, with magmatism enhanced by the development of the Caldas Tear, a slab window produced by subduction of the Sandra Ridge [48, 49]. According to the local interpretation of the AGC 2023 geological layer, the cave entrance occurs near the mapped contact between the Formación Combia and the Diorita de Támesis, also referred to as the Stock de Támesis (Figure 2, panel (c)). This intrusive body is described as predominantly dioritic, with local variations to quartz-diorite, quartz-monzodiorite, and amphibolic gabbro. The Atlas Geológico de Colombia 2023 assigns the Stock de Támesis to the late Miocene (Serravallian–Messinian) [50], with a formation age of approximately 9–10 Ma consistent with the regional Combia magmatic episode [48, 49]. An

earlier K–Ar age of 124 ± 6 Ma reported by González and Londoño [51] likely reflects incorporated older material rather than the crystallization age of the intrusive body. This mapped lithological contact may influence substrate heterogeneity and local hydrological pathways within the cave system.

Consistent with the organal model described for Antioquian pseudokarstic systems, the cave is structured by large rounded volcaniclastic boulders that form irregular walls, roofed passages, and discontinuous voids rather than dissolutional galleries. This architecture is expected to generate strong small-scale heterogeneity in light exposure, moisture, sediment accumulation, and rock-surface colonization, and to allow water movement through the overlying substrate to connect the cave interior with the surrounding montane landscape [28, 35, 47].

The cave spans a sharp environmental gradient rather than a continuously attenuating one. The transition from the semi-illuminated entrance to the fully aphotic interior occurs over short distances — approximately 30 m separate the entrance from the transition sector, and more than 80 m separate the entrance from the dark interior — and is governed primarily by the geometry of boulder accumulations rather than by gradual attenuation of light through open space. Air temperature across the interior sectors is stable and low (15.0–16.1 °C), with relative humidity consistently above 87% and rock-surface temperatures near 14 °C, contrasting sharply with the exterior environment immediately adjacent to the entrance (18.3 °C, 76% RH). These conditions place the cave within the psychrotolerant range, where organisms capable of growth at low temperatures but not necessarily requiring them are expected to be selectively favored [55, 56]. This thermal landscape has a direct methodological implication: targeting the low-temperature-tolerant component of the cultivable community requires incubation temperatures that approximate those of the cave interior.

Visible surface colonization occurs throughout the cave as pigmented films, hydrated patches, and laminated surface-associated structures on rock surfaces — green and orange films near the entrance, thinner mucilaginous structures on iron-stained rock in the transition sector, and faint whitish crusts on moist surfaces in the dark interior. These observations are consistent with the zonation framework established in the broader cave microbiology literature but have not been quantified or systematically characterized in any prior study of this system. To my knowledge, no microbiological investigation has been conducted in the Organal San Antonio, and no published study has examined cultivable microbial community structure in an organal-type cave. The combination of geological singularity, abrupt zonation, environmental stability, and minimal human impact makes the Organal San Antonio a suitable system for investigating how the cultivable microbial fraction varies across light-defined cave sectors in a tropical volcaniclastic context, and for establishing a first quantitative baseline against which future molecular, physiological, geochemical, and temporal studies can be compared.

1.5 Research question, objectives, and study design

This study asks whether the abrupt light-defined zonation of the Organal San Antonio is associated with differences in the cultivable microbial fraction detectable at the scale of a single

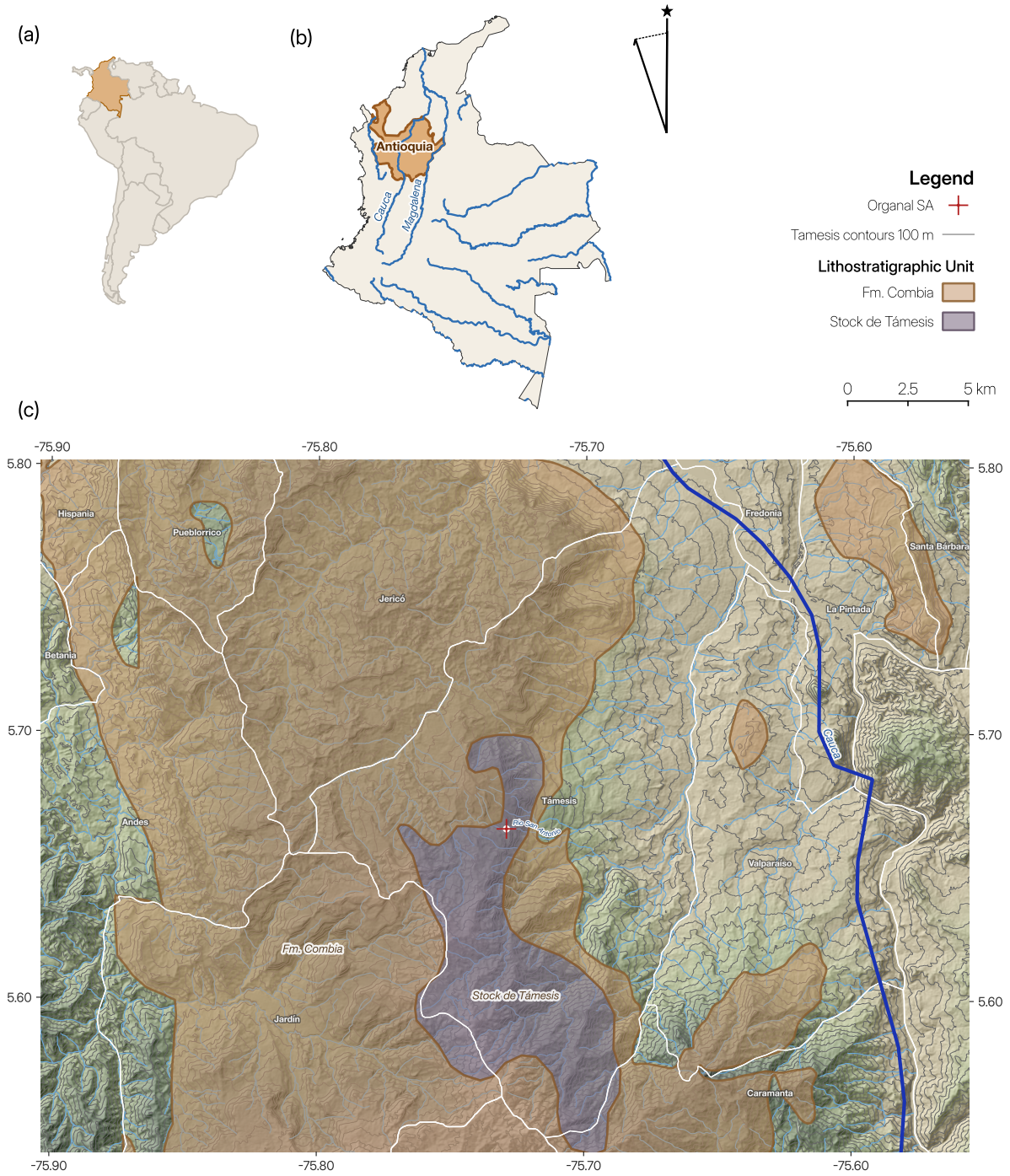

Figure 2. Geographic, topographic, and geological context of the Organal San Antonio. (a) South American context with Colombia highlighted. **(b)** Regional context showing the department of Antioquia within Colombia, with the Cauca and Magdalena rivers as geographic references. **(c)** Local topographic and geological context of the Támesis area. The cave entrance is marked at 5.664°N, 75.729°W, at approximately 2350 m a.s.l. Geological units include the Formación Combia (volcaniclastic basalts and andesites, Miocene) and the Diorita de Támesis or Stock de Támesis (predominantly dioritic intrusive, late Miocene; ~9–10 Ma). Terrain derived from the Copernicus Digital Elevation Model (GLO-30; [52]). Country, regional, and continental boundaries and base rasters from Natural Earth [53]; local political boundaries and hydrography from IGAC [54]; geological units from the Atlas Geológico de Colombia 2023 [50]. Local layers projected in MAGNA-SIRGAS 2018 / Origen-Nacional (EPSG:9377); graticules in WGS84 (EPSG:4326).

cave system. If sector-associated environmental filtering affects the R2A-recoverable community, cultivable community structure should partition with cave zonation, and that partitioning should be detectable in three complementary signatures (Figure 1): cultivable density per unit sediment, local morphotype-cluster diversity within samples, and compositional turnover among samples. If the zonation is instead ecologically transparent to the cultivable fraction — if cultivable density, diversity, and composition are indistinguishable across sectors — then either the environmental contrast does not strongly affect the cultivable fraction, or its effect does not reach the resolution accessible through the cultivation and morphotype-cluster framework used here.

The general objective is to characterize the cultivable microbial fraction along the light-defined ecological zonation of the Organal San Antonio and to determine whether sector identity is associated with differences in cultivable density, local morphotype-cluster diversity, and morphotype-level composition. The specific objectives are: (i) to quantify cultivable density across cave sectors defined by light availability and to test whether density changes along the gradient; (ii) to characterize morphotype-cluster composition and alpha diversity within each sector, assessing whether local diversity varies with zonation; (iii) to evaluate compositional turnover among sectors through multivariate community analysis, testing whether cultivable morphotype-cluster composition partitions with cave zonation; and (iv) to generate a preliminary phenotypic reference for selected cultivable representatives, assessing whether colony-level phenotypic clusters correspond to consistent cellular and biochemical profiles.

To address these objectives, the cultivable fraction was characterized through two independent experiments conducted at successive stages of the study: an initial binary contrast between illuminated and aphotic sectors, and a subsequent three-sector resolution of the full entrance-to-interior zonation. Both experiments used dilute R2A agar and colony morphotype classification as the primary framework for community-level analysis. Experiment II additionally employed cave-mimetic incubation conditions (14.5–15 °C), whereas Experiment I was incubated at ambient laboratory temperature (~20 °C). Together, these analyses establish, to my knowledge, the first quantitative cultivable baseline for an organal-type tropical volcaniclastic cave and provide the empirical foundation against which future molecular, physiological, geochemical, and temporal investigations of the Organal San Antonio can be positioned.

2 Materials and Methods

2.1 Study system and ecological zonation

Fieldwork was conducted in the Organal San Antonio, a tropical volcaniclastic pseudokarstic cave in the municipality of Támesis (Antioquia, Colombian Andes; ~2350 m a.s.l.; geological and environmental context described in Section 1). Three sectors were defined primarily on the basis of light availability, with associated abiotic conditions recorded during sampling: a semi-illuminated Entrance sector exposed to indirect external radiation and exhibiting stronger coupling with surface microclimate; a Transition sector, located approximately 30 m from the entrance, in which natural light is strongly attenuated but not entirely absent; and a fully aphotic

Dark sector, located more than 80 m from the entrance, in which natural illumination was undetectable during any sampling event. The transition between sectors is governed by the geometry of boulder accumulations rather than by gradual attenuation through an open linear passage. Light availability was classified qualitatively based on the presence or absence of detectable natural illumination.

Abiotic conditions were recorded *in situ* during sampling using a CHY820 thermohygrometer for air temperature and relative humidity; rock-surface temperature was recorded with the same field instrument configuration where applicable (Table 1). Sediment and cave-water pH were measured ex situ on 12 June 2025 using an Orion Star A111 pH meter (Thermo Scientific). Wet cave sediment yielded acidic values (pH 4.40 in both a sediment–water preparation and a dense sediment preparation), whereas filtered cave stream water was less acidic (pH 5.74). The post-autoclave pH of the diluted R2A medium used for cultivation was 7.01.

Table 1. *In situ* abiotic conditions recorded during sampling. Exterior values provide a surface reference for the interior gradient.

Sector	Air temperature (°C)	RH (%)	Rock temperature (°C)	Interior
Exterior	18.3	75.7	14.8	No
Entrance	15.0	92.7	14.2	Yes
Transition	16.1	87.5	14.1	Yes
Dark	15.2	92.0	13.9	Yes

2.2 Experimental structure and sampling

The cultivable community was investigated through two independent experiments conducted at successive stages of the study. Each experiment represents a distinct observational resolution of the cave's internal gradient, and inferences drawn from each are presented separately throughout the Results. Experiment I compared two operational categories — *Light* (the entrance and twilight portions, where residual photosynthetically active radiation could reach the substrate) and *Dark* (the fully aphotic interior) — with six independent biological replicates per category, yielding twelve sediment samples in total. Experiment II resolved the cave into three sectors (Entrance, Transition, Dark) with five independent biological replicates per sector, yielding fifteen sediment samples in total (Figure S1). A biological replicate is operationally defined as a single sediment collection point separated from all other replicates within the same category or sector by a minimum distance of approximately 70 cm and showing visible local variation in surface morphology, moisture retention, and colonization appearance. This definition treats each replicate as an independent observation of the cultivable community within its zone rather than as a subsample of a homogeneous patch. Substrate heterogeneity was evident within each sector: differences in rock inclination, porosity, mineral staining, moisture films, and the presence or absence of visible surface colonization were apparent across replicate positions, supporting the treatment of each collection point as an independent sample of the local microhabitat mosaic.

In both experiments, sampling targeted thin sediment layers and hydrated deposits closely associated with visible surface colonization on rock surfaces. Sediment was collected using

sterile nitrile gloves and sterile stainless-steel spatulas. The superficial field-moist sediment layer associated with visible colonization was gently scraped from the rock surface and transferred into sterile 1.5 mL microtubes. During fieldwork, spatulas were rinsed and cleaned between collection points using water available at the site and by scraping residual material from the tool surface; therefore, although cross-sample carryover was minimized, field cleaning should not be interpreted as full re-sterilization between samples. Contact with non-target surfaces was minimized throughout sampling. The sampling design included a complete set of backup field replicates; the final Experiment I workflow was initiated from these refrigerated backup samples 10 days after collection. For Experiment II, microbiological processing was initiated within 48 h of collection. In both cases, tubes were transported and maintained under refrigerated conditions until laboratory processing.

In Experiment II, each microtube was weighed before and after sediment addition using an analytical balance to obtain measured field-moist sediment mass per replicate (range: 1.25–1.89 g). In addition to cultivation-oriented samples, fresh sediment subsamples were collected for direct wet-mount observation using a Leica DM750 compound light microscope equipped with a FlexCam i5 camera, and rock fragments were retained for stereoscopic examination of mineral surfaces using a Carl Zeiss Stereo Discovery.V12 stereomicroscope equipped with an AxioCam. Environmental water was collected from the cave stream in sterile borosilicate glass bottles (Schott Duran), transported at 4 °C, and sterilized by autoclaving at 121 °C for 15 min prior to use as diluent in sediment suspensions and serial dilutions. Separately, fresh non-autoclaved cave stream water from the Dark sector was plated as an environmental water control, as described in Section 2.3.

2.3 Cultivation, dilution, and colony counting

A low-nutrient medium was used in both experiments to reduce nutrient shock and limit overgrowth by fast-growing copiotrophs. R2A agar powder (DM1962; Central Drug House (P) Ltd., New Delhi, India) was prepared at 25% of the manufacturer-recommended concentration (4.53 g/L total medium powder), supplemented with 15 g/L bacteriological agar powder (Biomark Laboratories, Pune, India) to ensure solidification at the reduced nutrient concentration, and 0.1 g/L $NaHCO_3$ as a minimal inorganic carbon source [41]. Media were autoclaved at 121 °C for 15 min; post-autoclave pH was 7.01. Media were dispensed into sterile Petri dishes and allowed to solidify at room temperature.

Plates from both experiments were followed through a shared observational sequence in which early colony emergence, primary colony counting, morphotype recognition, and subsequent isolate processing were treated as distinct stages. In Experiment I, plates were incubated at approximately 20 °C in a closed dark storage container under laboratory ambient conditions. In Experiment II, plates were incubated at 14.5–15 °C in total darkness in a laboratory cooling chamber (DVM Tecnología S.A.S.) equipped with a ventilation fan and cooling plate; temperature was monitored using a CHY820 thermohygrometer. This temperature regime approximates the *in situ* thermal conditions of the cave interior (Table 1) and was selected to

reduce bias toward faster mesophilic growth under warmer laboratory conditions. Small colonies became detectable during the first week of incubation, with visible emergence in Experiment II by approximately Day 4. The primary Experiment II colony census used for density and community analyses was recorded at Day 7, while morphotype recognition, colony-level verification, and isolate selection were consolidated progressively within approximately 10–20 days. Downstream purification, staining, microscopy, and cryopreservation were performed sequentially after this initial cultivation phase.

In both experiments, sediment was homogenized by vortexing for 30 s prior to dilution, and a mother suspension was prepared by resuspending 200 µL of field-moist sediment in 800 µL of autoclaved cave stream water. This produced a 1:5 sediment suspension in which the original sediment fraction was $0.2 = 2 \times 10^{-1}$. In Experiment I, this suspension was serially diluted from 10^{-1} through 10^{-5} in autoclaved cave stream water and spread-plated at 100 µL per plate onto 25% R2A agar. In Experiment II, the suspension was serially diluted to 10^{-1}, 10^{-2}, and 10^{-3}, with a technical replicate at 10^{-2} to assess within-sample counting variability.

For density estimation, one primary plate per biological replicate was selected by preferring countable plates (30–300 colonies) at the lowest dilution available (Tables S8–S9). The two experiments differed in their normalization denominator. In Experiment I, density was normalized volumetrically because no replicate-specific sediment mass was measured. In Experiment II, density was normalized gravimetrically using the estimated field-moist mass of the sediment aliquot used to prepare the mother suspension.

In Experiment II, the total field-moist sediment mass collected in each microtube was measured gravimetrically. Because the mother suspension was prepared from a standardized 200 µL aliquot of field-moist sediment rather than from the entire tube contents, the mass represented in the suspension was estimated as:

$$m_{\text{aliquot}} = m_{\text{tube}} \times \frac{V_{\text{aliquot}}}{V_{\text{tube}}}, \tag{1}$$

where m_{tube} is the measured field-moist sediment mass in the microtube, $V_{\text{aliquot}} = 0.2\,\text{mL}$ is the sediment volume used to prepare the mother suspension, and $V_{\text{tube}} \approx 1.5\,\text{mL}$ is the approximate field-moist sediment volume collected per tube. Thus, $m_{\text{aliquot}} = m_{\text{tube}} \times 0.2/1.5$. The resulting estimate is used as an aliquot-level gravimetric correction rather than as a direct measurement of the exact mass of the 200 µL aliquot. This calculation assumes uniform bulk density within the tube after vortexing; any deviation from this assumption introduces an estimation error that is expected to be small relative to the roughly one-order-of-magnitude difference in cultivable density observed between sectors. Per-replicate m_{tube} and derived m_{aliquot} values used in Equation 2 are reported in Table S10.

Cultivable density was calculated as:

$$\text{CFU per unit substrate} = \frac{N}{D_{\text{serial}} \times V_{\text{plated}} \times A}, \tag{2}$$

where N is the colony count on the selected plate, D_{serial} is the plated serial dilution, $V_{\text{plated}} = 0.1\,\text{mL}$ is the volume spread-plated, and A is the substrate amount represented in the plated dilution series. In Experiment I, $A = 0.2\,\text{mL}$ wet sediment represented in the mother suspension, and results are expressed as CFU mL^{-1} wet sediment. In Experiment II, $A = m_{\text{aliquot}}$, the estimated field-moist sediment mass used to prepare the mother suspension, and results are expressed as CFU g^{-1} field-moist sediment. This formulation separates the serial dilution applied after the mother suspension from the substrate normalization denominator and makes explicit that the Experiment II gravimetric correction is based on the processed sediment aliquot rather than on the full tube mass.

Fresh non-autoclaved cave stream water collected from the Dark sector was plated separately as an environmental water control to estimate the cultivable background associated with the water source itself. This control was distinct from the autoclaved cave stream water used as sterile diluent for sediment suspensions and serial dilutions and was not treated as a sterility test of the diluent (Table S6). A negative control consisting of the autoclaved cave stream water used as diluent was plated in parallel in both experiments; no colony growth was recorded.

2.4 Morphotype classification and cross-sector crosswalk

Colony morphotypes were defined operationally on the basis of macroscopic colony characteristics observed on the plate surface: pigmentation, opacity, surface texture (matte versus glistening or mucoid), elevation profile, margin architecture, colony size, transparency, and spreading behavior. A morphotype, as used in this study, is the smallest visually distinguishable category of colony phenotype that could be consistently recognized across plates within a given experiment. The defensibility of this unit rests on empirical validation showing that colony morphology can recover coarse but meaningful phenotypic structure in environmental cultivation studies, while also acknowledging that morphological convergence may collapse taxonomically distinct organisms and phenotypic plasticity may split related organisms across colony forms [45, 46]. Morphotypes are therefore treated here as operational phenotypic units rather than taxonomic assignments.

In Experiment I, morphotypes were assigned globally across both Light and Dark categories, yielding nineteen described codes (ORG-SA001 through ORG-SA019; Table S1). Fourteen of these were detected in countable plates and included in the Experiment I community matrix. Representative colonies were re-streaked onto fresh 25% R2A agar plates until morphological consistency across successive generations suggested adequate purification. Purified isolates were cryopreserved at −80 °C in 30% (v/v) glycerol prepared with autoclaved cave stream water.

In Experiment II, morphotypes were classified independently within each sector: fifteen codes for the Entrance sector (E-MT01 through E-MT15, including three putative fungal morphotypes), fourteen for Transition (T-MT01 through T-MT14, including two putative fungal morphotypes), and thirteen for Dark (D-MT01 through D-MT13, including one putative fungal morphotype), for a total of forty-two zone-specific sediment morphotype codes (Tables S2–S4). Fresh cave-water

control morphotypes were coded separately as C-MT01 through C-MT06 and were not included in the sediment community matrix (Table S6).

To enable cross-sector community comparison in Experiment II, the forty-two zone-specific sediment morphotype codes were mapped onto a unified set of twenty-three operational phenotypic clusters (CL01–CL23) using a diagnostic crosswalk based on pigmentation, opacity, shape, elevation, margin architecture, size, surface texture, transparency, mucoidity, and spreading behavior (Table S5). Assignment confidence was recorded as High, Moderate, or Low according to the number, distinctiveness, and reproducibility of shared diagnostic traits. High-confidence assignments required multiple strongly discriminating shared characters; moderate-confidence assignments reflected a recognizable shared phenotype with minor variation in secondary traits; low-confidence assignments represented zone-restricted phenotypes or cases in which phenotypic similarity to another cluster required cautious interpretation.

The final crosswalk comprised seven cross-sector clusters treated as bacterial at the colony-catalogue stage (CL01–CL04, CL06–CL08), two bacterial clusters shared by two sectors (CL05 and CL14), eleven zone-restricted sediment clusters (CL09–CL13, CL15–CL19, CL23), and three putative fungal clusters (CL20–CL22). All twenty-three clusters were retained in the community matrix. Subsequent isolate-level characterization did not modify the crosswalk or the community matrix. Zone-restricted clusters were treated as biologically informative structural absences from non-source sectors rather than as missing data [57, 58]. All downstream community analyses are therefore interpreted at the morphotype-cluster level.

2.5 Phenotypic characterization of representative isolates

Twenty-three isolates from Experiment II — eight from the Entrance sector, six from Transition, seven from Dark, and two fresh cave-water control isolates — were selected for preliminary phenotypic characterization. Selection prioritized phenotypic distinctness and included representatives of both cross-sector and zone-restricted clusters. Isolates were purified by sequential re-streaking on 25% R2A agar to single-colony morphological consistency prior to characterization. Gram-stained preparations were examined using a Leica DM750 compound light microscope equipped with a FlexCam i5 camera. Colony morphology and plate-level appearance were examined stereoscopically using a Carl Zeiss Stereo Discovery.V12 stereomicroscope equipped with an AxioCam.

The characterization battery comprised three assays. (i) Gram staining was performed using the standard four-reagent protocol (crystal violet, Gram's iodine, ethanol decolorization, and safranin counterstain) on cells taken from actively growing low-temperature cultures on 25% R2A agar, generally after approximately six days of incubation and, for slower-growing isolates, up to approximately ten days. This culture-age range reflects the slower development of cave-derived colonies under low-temperature cultivation and was taken into account when interpreting ambiguous or peripheral staining patterns. Smears were heat-fixed, stained, and examined by oil-immersion light microscopy at a total magnification of ×1000 for Gram reaction, cell morphology, approximate cell dimensions, and cellular arrangement. At least two independent staining

preparations were performed per isolate where sufficient biomass was available; where results were inconsistent, additional preparations were examined until a reproducible assignment could be made or the ambiguity was formally recorded. (ii) The 3% KOH string test was performed as an independent confirmatory assay for Gram classification: colony material was suspended in a drop of 3% KOH on a glass slide and stirred continuously for 30 s, and the formation of a viscous string upon lifting the inoculation loop was interpreted as consistent with a Gram-negative cell envelope [59]. In cases of discordance between Gram staining and the KOH string test, the consolidated assignment was resolved by retaining the higher-confidence primary observation, while both raw outcomes were recorded in the detailed characterization record (Table S7). (iii) Catalase activity was assessed by applying a drop of 3% H_2O_2 directly to a small amount of colony material on a glass slide; vigorous and immediate effervescence was interpreted as a positive result.

Three isolates — E-MT10, D-MT04, and D-MT08 — were excluded from the consolidated bacterial phenotypic profile. E-MT10 did not yield reliable Gram, KOH, or catalase information; D-MT04 produced heterogeneous cellular material consistent with an unresolved or potentially mixed preparation; and D-MT08 did not yield confidently visualized bacterial cells during Gram-stain review and was therefore treated as a putative fungal morphotype for the purposes of post-cultivation characterization. These exclusions apply only to the isolate-level characterization layer: the corresponding colony morphotypes remain retained in the morphotype catalogue, cross-sector crosswalk, and community matrix wherever applicable. Lactophenol staining was attempted for selected putative fungal morphotypes, but preparations yielded fragmented material without diagnostic fungal structures; these colonies were therefore retained as putative fungal morphotypes based on colonial macromorphology rather than assigned as confirmed fungal taxa. Following characterization, all isolates that achieved morphological purity were cryopreserved at −80 °C in 30% (v/v) glycerol prepared with autoclaved cave stream water, joining the reference collection established in Experiment I.

2.6 Statistical analysis

All statistical analyses were conducted in R (v4.5.2) using the `tidyverse` ecosystem for data management and visualization, `vegan` (v2.7-3) for community-level analyses [60], `iNEXT` (v3.0.2) for rarefaction-based diversity estimation [61], and `effectsize` (v1.0.2) for standardized effect-size calculation [62]. Effect sizes with 95% confidence intervals are treated as the primary inferential tool, with p-values reported as auxiliary evidence [63]; exact values for all tests are reported throughout.

Cultivable density values were $\log_{10}$-transformed prior to all parametric tests. In both experiments, the assumptions of normality (Shapiro–Wilk test on model residuals) and homoscedasticity (Levene test) were evaluated prior to parametric analysis. In Experiment I, Shapiro–Wilk rejected normality ($p = 0.038$); the Wilcoxon rank-sum test was therefore treated as the primary test, with the Welch t-test as corroboration. Hedges' g with 95% confidence intervals was computed as the standardized effect size. In Experiment II, both assumptions were satisfied

(Shapiro–Wilk $p = 0.345$; Levene $p = 0.660$); one-way ANOVA was the primary test, with the Kruskal–Wallis test as non-parametric corroboration. Post-hoc pairwise comparisons used Welch t-tests with Benjamini–Hochberg correction; Hedges' g with 95% confidence intervals was computed for all three pairwise contrasts.

Alpha diversity was characterized per replicate by morphotype richness (observed count of distinct morphotype codes in Experiment I and phenotypic clusters in Experiment II), Shannon entropy (H'), and Simpson's complement ($1 - D$). Between-sector comparisons followed the same parametric–non-parametric framework; for Simpson's complement in Experiment II, where residuals failed the normality assumption (Shapiro–Wilk $p = 0.010$), the Kruskal–Wallis test was treated as primary.

Beta diversity was assessed through multivariate analysis of the sample-by-morphotype abundance matrix in Experiment I and the sample-by-cluster abundance matrix in Experiment II. The Experiment I matrix comprised twelve samples and fourteen morphotypes; the Experiment II matrix comprised fifteen samples and twenty-three operational phenotypic clusters. Abundance matrices were Hellinger-transformed prior to computing Bray–Curtis dissimilarities, reducing the dominance of highly abundant morphotypes while retaining information from rarer phenotypic units [57]. Samples were ordinated by non-metric multidimensional scaling (NMDS; `metaMDS`, `vegan`). Compositional differences among groups were tested with permutational multivariate analysis of variance (PERMANOVA; 999 permutations; `adonis2`, `vegan`) [64].

Because PERMANOVA is sensitive to heterogeneity in within-group multivariate dispersion, each PERMANOVA was preceded by a permutation test for homogeneity of multivariate dispersion (`betadisper` and `permutest`, `vegan`) [58]. Where betadisper was non-significant, the PERMANOVA result was interpreted primarily as compositional separation among group centroids. Where betadisper was significant, the result was interpreted conservatively as potentially confounded by dispersion heterogeneity. Pairwise PERMANOVA contrasts in Experiment II were computed with Benjamini–Hochberg correction applied to permutation p-values. SIMPER analysis (`simper`, `vegan`) was used only as a descriptive tool to identify the phenotypic clusters contributing most to between-sector dissimilarity and was not used as inferential evidence.

Quality-control metrics for Experiment II were evaluated at three levels. Colony-count concordance was assessed by comparing the sum of morphotype-assigned counts with the independently recorded total colony count for each plate. Where discrepancies occurred, the morphotype-sum count was used as the internally consistent abundance total for downstream morphotype-based community analyses, while the original total count was retained as an auditable primary record. Technical-replicate concordance was evaluated for the plate pairs produced at the 10^{-2} dilution. Fresh cave-water background was evaluated separately from diluent sterility: the autoclaved cave stream water used as diluent was plated as a negative control, whereas fresh non-autoclaved cave stream water was plated independently to estimate the cultivable load associated with the water source itself (Table S6).

3 Results

3.1 Field observations and colony emergence

Sampling across the Organal San Antonio revealed a spatially structured pattern of visible surface colonization consistent with the cave's light-defined zonation (Figure 3). In the Entrance sector, hydrated rock surfaces near the zone of external light incidence showed localized greenish tones, darkened moist patches, and visible colonization associated with fine sediment accumulations and boulder-contact zones. The Transition sector was characterized by more conspicuous orange-toned and translucent surface films, often mucilaginous in appearance and concentrated along seepage pathways between boulders where water was visibly arriving from the surface through the overlying substrate. The fully aphotic Dark sector displayed the sparsest visible colonization, with faint pale films and crust-like deposits restricted to persistently moist surfaces and without the green or orange pigmentation observed in illuminated or semi-illuminated sectors. In all three sectors, visible surface colonization was spatially discontinuous and concentrated in microhabitats defined by the intersection of moisture, sediment retention, and substrate roughness rather than uniformly distributed across rock surfaces. No quantitative taxonomic or chemical characterization of these surface features was performed; they are reported as qualitative contextual observations.

Direct observation of fresh sediment wet mounts using compound light microscopy revealed diatom frustules, ciliate-like unicellular eukaryotes, and cyst-like structures, primarily in Entrance-sector samples (Figure 3a). These visual identifications were not resolved to lower taxonomic rank and were used only as qualitative ecological context. They indicate that the sediment-associated microhabitat harbors a broader eukaryotic assemblage beyond the cultivable bacterial and putative fungal fraction targeted by the cultivation workflow. Stereoscopic examination of rock fragments further showed visible heterogeneity in surface coloration and texture across sectors, including surface coatings and mineral deposits of different appearance on Transition and Dark-sector substrates. The nature and composition of these deposits were not further characterized.

Incubation of plated sediment suspensions on dilute R2A agar produced visible colonies within the first week in both experiments, with early colony emergence especially evident in Experiment II by approximately Day 4 and the richest countable growth generally observed at intermediate dilutions. Colony fields became progressively more interpretable over the subsequent observation window, allowing primary colony counts, morphotype recognition, and isolate selection to be treated as sequential rather than simultaneous steps. In Experiment II, counted at Day 7 under cave-mimetic temperature, the cultivable assemblages were already visually distinct among sectors at the plate level. Entrance and Transition plates produced dense, phenotypically heterogeneous colony fields dominated by transparent punctiform colonies and pale cream circular forms, with occasional pigmented types; Dark plates produced consistently sparser colony fields in which the same general operational morphotype set was recognizable but at visibly reduced abundance. Putative fungal morphotypes, when present, formed the

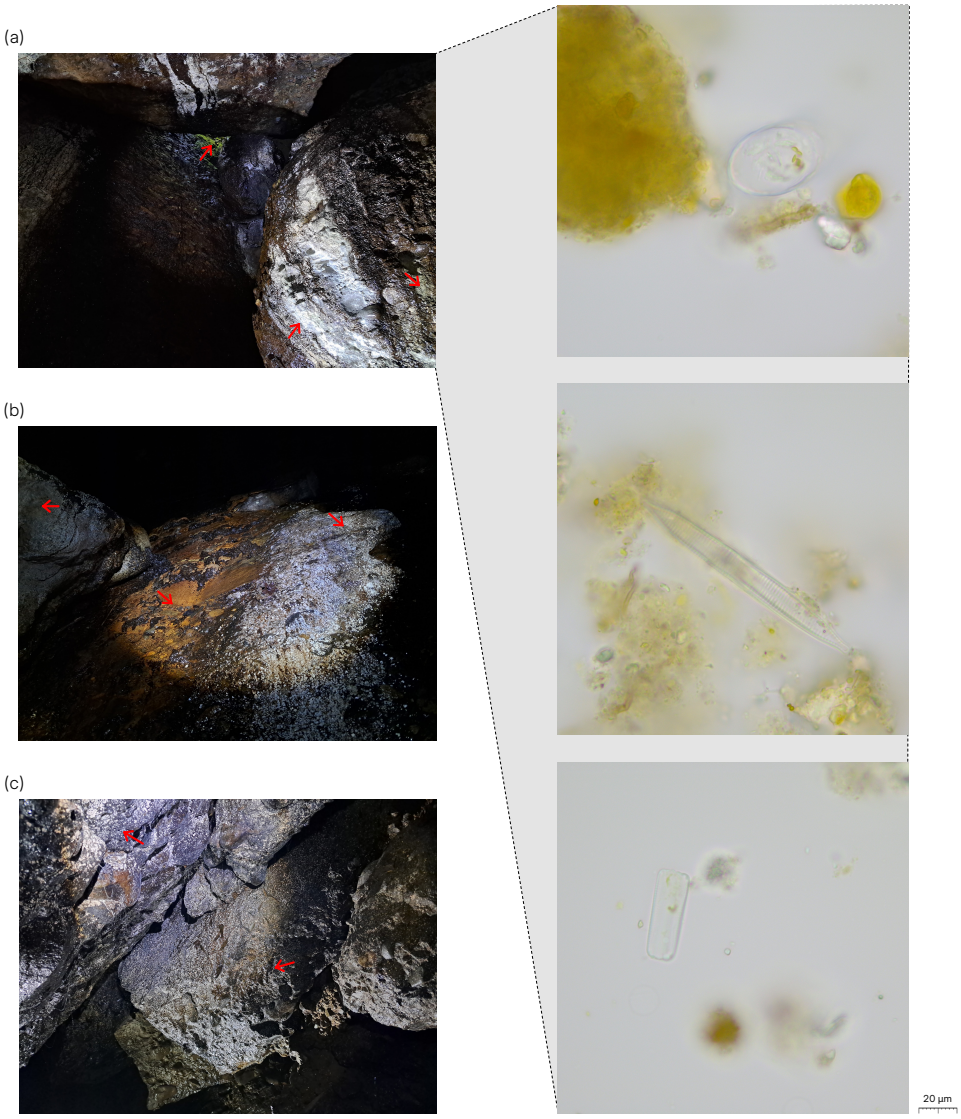

Figure 3. Field-scale microhabitats and fresh-sediment microscopy across the Organal San Antonio cave gradient. (a) Entrance sector, showing a hydrated rock corridor near the zone of external light incidence; red arrows indicate selected surfaces and contact zones where moisture, sediment retention, and localized colonization were observed. The associated microscopy panels show representative fresh-sediment wet mounts from Entrance-sector material observed with the Leica compound light microscope, including a ciliate-like unicellular eukaryote and diatom frustules recognized by visual inspection. **(b)** Transition sector, showing moist boulder surfaces with orange-toned and pale surface films concentrated along seepage-associated microhabitats. **(c)** Dark sector, showing aphotic rock surfaces with sparse pale coatings or crust-like deposits restricted to persistently moist areas. Microscopic observations were not resolved to lower taxonomic rank, and the field-scale features indicated by red arrows were used only as qualitative ecological context rather than as quantified sampling points or inputs to the cultivable community matrix.

slowest-growing component of the assemblage in each sector and remained a minor fraction of the total colony count.

3.2 The morphotype catalogue

Colony morphotype classification produced a stable phenotypic vocabulary for each experiment. Experiment I yielded nineteen globally assigned morphotypes (ORG-SA001 through ORG-SA019; Table S1), of which fourteen were detected on the twelve plates analyzed for community-level statistics; the remaining five appeared only in non-countable or excluded plates and were not included in the Experiment I abundance matrix.

Experiment II produced a higher-resolution catalogue of forty-two zone-specific sediment morphotype codes distributed across the three sectors: fifteen in Entrance (including three putative fungal types), fourteen in Transition (two putative fungal types), and thirteen in Dark (one putative fungal type). The complete zone-specific catalogues are presented in Tables S2–S4. These codes were mapped onto a unified set of twenty-three operational phenotypic clusters (CL01–CL23) through the cross-sector crosswalk described in Section 2.4 and detailed in Table S5. The crosswalk comprised seven cross-sector clusters treated as bacterial at the colony-catalogue stage (CL01–CL04, CL06–CL08), two bacterial clusters shared by two sectors (CL05, CL14), four Entrance-restricted clusters (CL11–CL13, CL23), three Transition-restricted clusters (CL09, CL10, CL19), four Dark-restricted clusters (CL15–CL18), and three putative fungal clusters (CL20–CL22). All twenty-three clusters were retained in the community matrix used for compositional analyses. Subsequent isolate-level characterization did not modify the crosswalk or the community matrix.

Fresh cave-water control morphotypes were coded separately as C-MT01 through C-MT06 and were not included in the sediment community matrix. Their correspondence to sediment-associated phenotypic clusters is reported in the crosswalk only as environmental background information (Tables S5 and S6).

3.3 Cultivable density along the light-defined gradient

Cultivable density varied substantially along the cave's light-defined zonation in both experiments. In Experiment I, the mean cultivable density was higher in the Light category (5.60×10^5 CFU mL^{-1} wet sediment) than in the Dark category (2.69×10^5 CFU mL^{-1} wet sediment), corresponding to an approximately twofold difference on the linear scale. The Light category displayed substantially greater variability among replicates on the $\log_{10}$ scale (SD = 0.382 versus 0.058), a pattern traceable in part to one low-density replicate (35 colonies) within the Light set. Shapiro–Wilk testing rejected normality of residuals ($W = 0.851$, $p = 0.038$), and the non-parametric Wilcoxon rank-sum test was therefore given interpretive priority. Neither the Wilcoxon test ($W = 30$, $p = 0.066$) nor the Welch t-test ($t = 2.015$, df = 5.2, $p = 0.098$) reached significance at $\alpha = 0.05$. The standardized effect size was large (Hedges' $g = 1.16$; 95% CI: −0.10 to 2.38), with the confidence interval narrowly crossing zero. The direction of the difference was consistent with lower cultivable density in the aphotic interior, but the contrast did not resolve statistically at the sample size of this experiment.

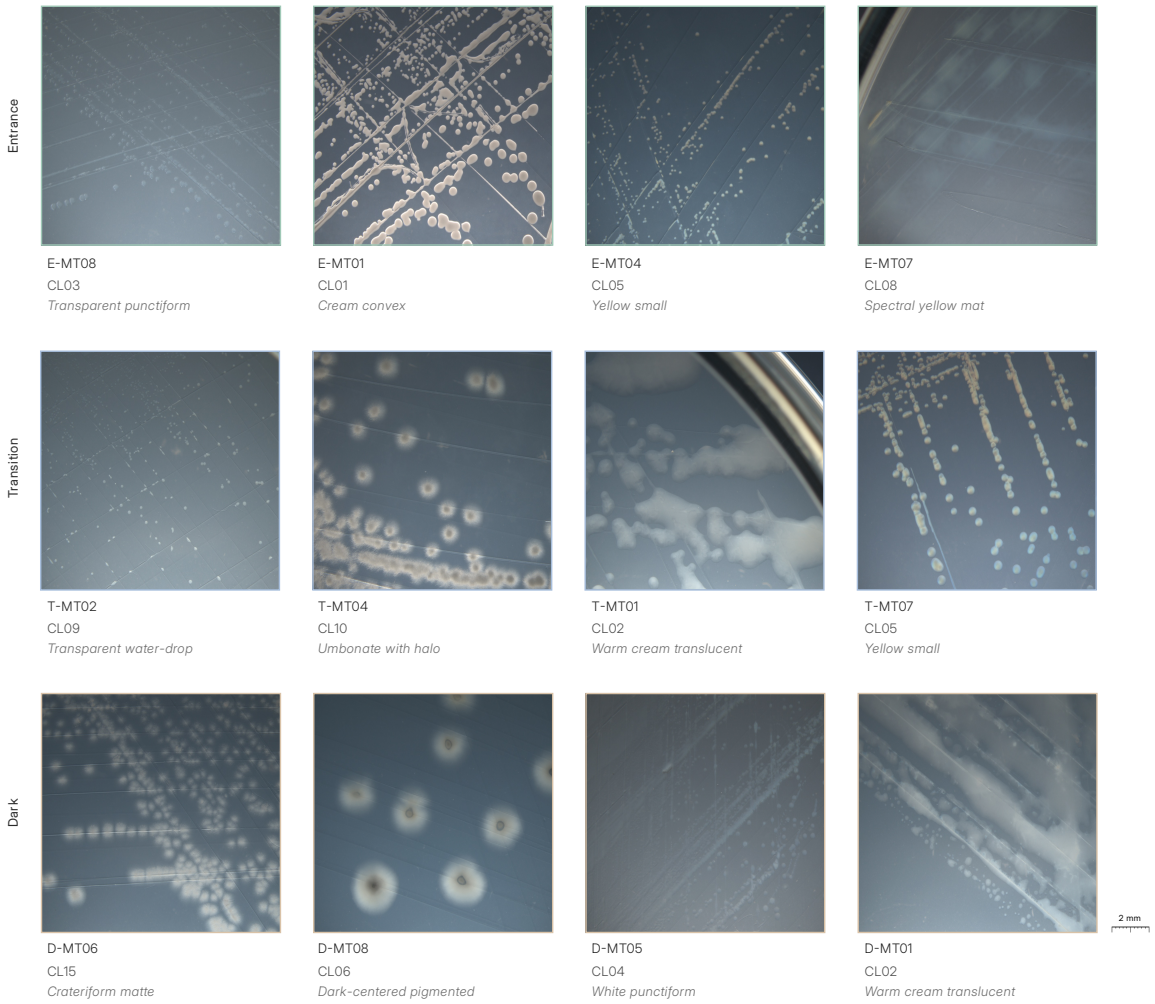

Figure 4. Representative cultivable morphotypes recovered from the Organal San Antonio. Panels show selected colony morphotypes from the Entrance, Transition, and Dark sectors, labeled with their sector-specific morphotype code and final operational phenotypic cluster. The gallery is representative rather than exhaustive; the complete morphotype catalogues and cross-sector phenotypic crosswalk are provided in Tables S2–S4 and Table S5. Selected panels illustrate dominant, shared, zone-restricted, or visually diagnostic phenotypes used to support the morphotype-level community analysis. Because photographs were acquired across different observation dates and illumination settings, differences in brightness, contrast, or apparent color intensity among panels should not be interpreted as diagnostic differences unless explicitly described in the morphotype catalogue or crosswalk.

Experiment II, conducted with aliquot-level gravimetric normalization and three-sector resolution, recovered a clearer and more precisely structured pattern. Cultivable density followed a step-like pattern across sectors (Figure 5a; Table 2): the Entrance and Transition sectors supported statistically indistinguishable densities of approximately 5.1×10^5 and 5.6×10^5 CFU g^{-1} field-moist sediment, respectively, while the Dark sector supported approximately 8.9×10^4 CFU g^{-1} field-moist sediment — a reduction of roughly sixfold. One-way ANOVA confirmed a significant sector effect ($F_{2,12} = 11.27$, $p = 0.0018$; $\eta^2 = 0.652$), corroborated by the Kruskal–Wallis test ($H = 7.58$, $p = 0.0226$). Post-hoc pairwise comparisons (Welch t, BH-adjusted) showed that Entrance and Transition did not differ from each other ($p = 0.829$; Hedges' $g = -0.144$; 95% CI: −1.381 to 1.102), while both differed from the Dark sector (Entrance–Dark: $p = 0.0135$, $g = 2.707$, 95% CI $[0.871, 4.467]$; Transition–Dark: $p = 0.0135$, $g = 2.224$,

95% CI [0.548, 3.824]). One replicate within the Dark sector (D-R1, $\log_{10}$ = 5.630) produced a density value within the range of the illuminated sectors; this replicate was retained in all reported analyses. The Transition sector also showed higher within-sector variability than the Entrance (SD = 0.334 versus 0.114 on the $\log_{10}$ scale), which may reflect microenvironmental heterogeneity among replicate positions along the seepage-fed Transition corridor, though this remains unverified.

Table 2. Cultivable density ($\log_{10}$ CFU g^{-1} field-moist sediment) across the three sectors in Experiment II (n = 5 per sector). Values use aliquot-level gravimetric normalization based on the estimated field-moist mass of the 200 µL sediment aliquot used to prepare the mother suspension.

Sector	n	Mean	SD	Min	Max
Entrance	5	5.712	0.114	5.563	5.826
Transition	5	5.748	0.334	5.217	6.059
Dark	5	4.951	0.381	4.758	5.630

Across both experiments, the direction of the density signal is consistent: cultivable density was lower in the aphotic interior than in sectors receiving residual light. Experiment I detected this direction as a large-effect signal that did not resolve statistically at the available sample size; Experiment II resolved it as a strong sector-associated density contrast, with sector identity explaining approximately 65% of the variance in cultivable density. The aliquot-level gravimetric correction changes the absolute CFU g^{-1} scale but does not affect the relative sector pattern or the inferential statistics.

3.4 Local morphotype diversity did not show detectable sector-level differences

Local diversity, quantified at the scale of individual replicates, did not show detectable differences among sectors in either experiment. In Experiment I, morphotype richness, Shannon diversity H', and Simpson complement $1 - D$ were statistically indistinguishable between Light and Dark categories (richness: Welch $p = 0.134$, Wilcoxon $p = 0.111$; Shannon: Welch $p = 0.797$; Simpson: Welch $p = 0.292$). The two categories supported comparable numbers of morphotypes at comparable evenness.

In Experiment II, the same pattern held across the three-sector resolution (Table 3; Figure 5b–d). Each sector supported approximately 10–11 phenotypic clusters per replicate at comparable evenness (Shannon H' between 1.72 and 1.88). One-way ANOVA revealed no detectable sector effect for morphotype-cluster richness ($F = 0.236$, $p = 0.793$; Kruskal–Wallis $H = 0.538$, $p = 0.764$) or for Shannon diversity ($F = 0.810$, $p = 0.468$; Kruskal–Wallis $H = 2.18$, $p = 0.336$). Shapiro–Wilk testing rejected normality of Simpson complement residuals ($p = 0.0098$); the Kruskal–Wallis test was therefore treated as the primary test for this metric and was likewise non-significant ($H = 2.16$, $p = 0.340$). The absence of a detectable sector-level effect was robust to the inclusion or exclusion of putative fungal morphotypes.

Together with the density findings, this result indicates a specific dissociation: sectors differed substantially in how many colonies were recovered per unit sediment, but did not show detectable differences in how many phenotypic clusters were represented within a

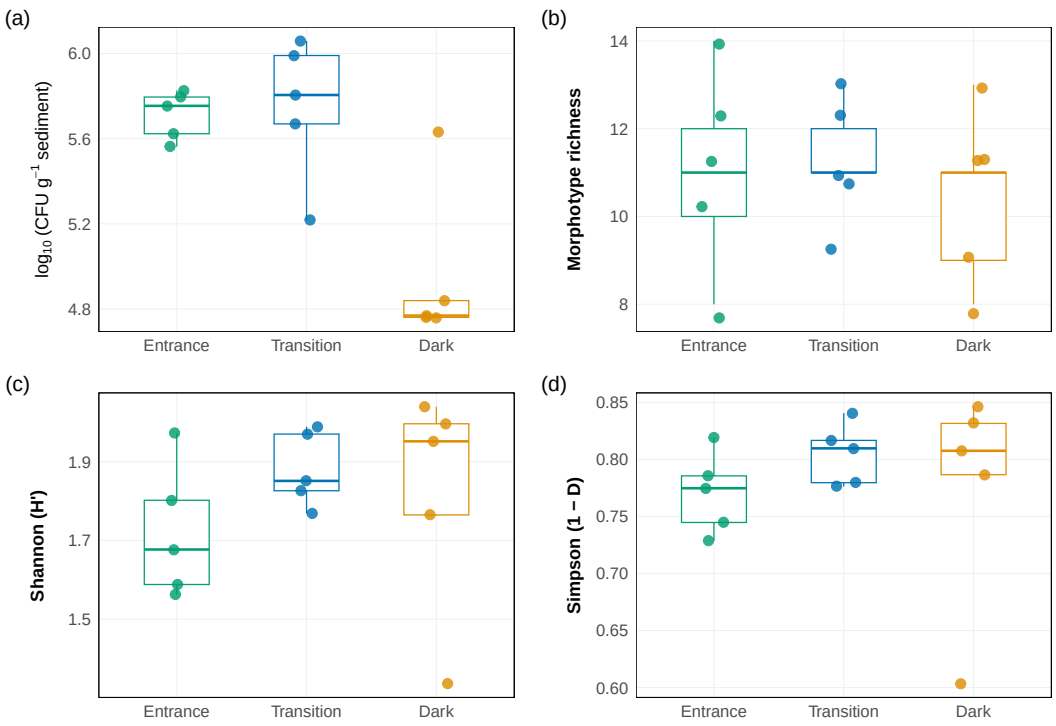

Figure 5. Cultivable density and local diversity across light-defined cave sectors in Experiment II. **(a)** $\log_{10}$(CFU g^{-1} field-moist sediment) across the three sectors, calculated using aliquot-level gravimetric normalization, with individual replicate values overlaid on box plots. Overall ANOVA: $F_{2,12} = 11.27$, $p = 0.0018$, $\eta^2 = 0.652$. **(b)** Morphotype-cluster richness. **(c)** Shannon diversity H'. **(d)** Simpson complement $1 - D$. No local diversity metric showed a detectable sector-level difference (all $p > 0.33$). The contrast between panel (a) and panels (b–d) visualizes the dissociation between cultivable density and local morphotype-cluster diversity.

Table 3. Alpha diversity of the cultivable community across cave sectors in Experiment II (mean ± SD; $n = 5$ per sector). N_{total} is the mean effective colony count per replicate used in diversity calculations.

Sector	Observed richness	Shannon H'	Simpson $1 - D$	N_{total}
Entrance	11.0 ± 2.2	1.720 ± 0.169	0.771 ± 0.035	233 ± 69
Transition	11.2 ± 1.5	1.881 ± 0.095	0.805 ± 0.027	227 ± 87
Dark	10.4 ± 1.9	1.818 ± 0.289	0.775 ± 0.098	163 ± 28

sample. The additional cultivable density recovered in the Entrance and Transition sectors was therefore not accompanied by a corresponding increase in local morphotype-cluster richness or evenness. Sample-size-based rarefaction and extrapolation curves supported this interpretation by indicating that morphotype-cluster richness was reasonably captured at the observed colony counts across Experiment II replicates (Figure S2).

3.5 Compositional turnover across the light-defined gradient

Compositional turnover among replicates was analyzed through Bray–Curtis dissimilarities computed on Hellinger-transformed abundance matrices. In Experiment I, PERMANOVA on the 12-sample, 14-morphotype matrix detected a category effect ($R^2 = 0.227$, $F = 2.94$, $p = 0.021$). The betadisper test, however, was also significant ($F = 5.39$, permutation $p = 0.021$), indicating that the Light category was substantially more heterogeneous in multivariate space than the

Dark category (mean within-category Bray–Curtis dissimilarity: 0.352 versus 0.114). Under these conditions, the compositional signal cannot be attributed cleanly to centroid displacement alone; it likely reflects a combination of compositional differentiation and differential within-category dispersion. SIMPER analysis identified five morphotypes accounting for 73% of the between-category dissimilarity, all more abundant in the Light category (ORG-SA019: 15.5%; ORG-SA001: 9.6%; ORG-SA015: 7.2%; ORG-SA009: 7.0%; ORG-SA002: 5.5%). The dominant pattern was quantitative reduction — the same morphotypes at systematically lower abundance in the Dark — rather than qualitative replacement. Figures S3 and S4 present the statistical outputs for Experiment I.

Experiment II, conducted on the 15-sample, 23-cluster matrix derived from the final cross-sector phenotypic crosswalk, resolved compositional structure with higher statistical clarity. PERMANOVA detected a strong sector effect ($R^2 = 0.573$, $F = 8.06$, $p = 0.001$; Figure 6a; Table 4), with all three pairwise contrasts remaining significant after Benjamini–Hochberg correction (Entrance–Transition: $R^2 = 0.509$, $p_{adj} = 0.016$; Entrance–Dark: $R^2 = 0.539$, $p_{adj} = 0.016$; Transition–Dark: $R^2 = 0.466$, $p_{adj} = 0.016$; the tied adjusted values reflect the joint floor imposed by 999 permutations and three-way BH correction). Betadisper was non-significant (permutation $p = 0.334$; ANOVA $p = 0.319$), indicating that the sector effect was not explained by differential within-sector dispersion. NMDS ordination (stress = 0.092) recovered visually separated sector groupings in phenotypic-cluster space.

Table 4. PERMANOVA and betadisper results for cultivable community composition in Experiment II (23-cluster crosswalk; Hellinger-transformed Bray–Curtis; 999 permutations). Permutation p-values are reported; ANOVA p is provided for betadisper as supplementary evidence.

PERMANOVA					
Term	Df	Sum of Sq.	R^2	F	p
Sector	2	0.787	0.573	8.06	0.001
Residual	12	0.586	0.427		
Total	14	1.373	1.000		
Betadisper					
Test		F	p		
ANOVA		1.257	0.319		
Permutation		1.257	0.334		

Seven cross-sector phenotypic clusters treated as bacterial at the colony-catalogue stage (CL01–CL04, CL06–CL08) were detected in all three sediment sectors, constituting a shared cultivable core whose abundances varied quantitatively across the gradient. CL03 (transparent punctiform), the most abundant cluster overall, declined in mean replicate count from 75.6 in Entrance to 52.2 in Transition and 36.0 in Dark, tracking the overall density pattern (Figure 6c). No cross-sector cluster was absent from any sediment sector, indicating that this shared phenotypic core persisted throughout the cave under the cultivation conditions used.

Superimposed on this shared core, each sector contained zone-restricted phenotypic clusters absent from adjacent sectors. The Entrance sector contained four restricted clusters (CL11–CL13,

CL23) at low overall abundance, contributing approximately 5.6% of the Entrance community. The Dark sector contained four restricted clusters (CL15–CL18) at moderate abundance, contributing approximately 22.4% of the Dark community. The Transition sector contained three restricted clusters (CL09, CL10, CL19) at substantial abundance, together contributing approximately 26.9% of the Transition community. CL09 (mean 31.6 colonies per replicate) and CL10 (mean 22.8) together accounted for approximately 24% of all individuals recovered from the Transition sector and were absent from both Entrance and Dark.

SIMPER analysis identified distinct contributions to each pairwise comparison and is treated here as descriptive rather than inferential evidence. The Entrance–Dark contrast was driven primarily by abundance reductions in shared clusters: CL03 (9.7%, $p = 0.033$) and CL04 (9.4%, $p = 0.059$) were the two leading contributors through quantitative reduction, with the Dark-restricted CL15 contributing 7.2% ($p = 0.009$) through qualitative turnover. The Transition–Dark contrast was driven by reciprocal zone-restricted replacement: CL15 (Dark-restricted, 7.5%, $p = 0.002$) and CL09 (Transition-restricted, 7.4%, $p = 0.001$) were the leading contributors. The Entrance–Transition contrast was dominated by shared-cluster abundance shifts (CL04: 8.3%, $p = 0.178$; CL03: 7.5%, $p = 0.540$; CL02: 6.6%, $p = 0.185$), alongside the contribution of the Transition-restricted CL09 (6.4%, $p = 0.006$) and the Transition-enriched CL07 (4.8%, $p = 0.037$).

Across both experiments, compositional turnover was detected but resolved with different degrees of analytical clarity. Experiment I provided an exploratory binary signal whose interpretation is limited by significant dispersion heterogeneity. Experiment II resolved the compositional signal as sector-associated turnover in the 23-cluster matrix, with sector identity accounting for more than half of the variance. The Transition sector was not simply an intermediate compositional blend of Entrance and Dark; it supported its own characteristic set of restricted phenotypic clusters at substantial abundance.

3.6 Phenotypic characterization of representative isolates

Twenty-three isolates from Experiment II — eight from Entrance, six from Transition, seven from Dark, and two fresh cave-water controls — were subjected to preliminary phenotypic characterization through Gram staining, 3% KOH string test, catalase assay, and light microscopy. The main-text summary reports the consolidated profiles of sediment-derived isolates retained in the bacterial phenotypic profile (Table 5), whereas the complete per-test record, including fresh cave-water controls, raw KOH outcomes, confidence levels, and characterization notes, is provided in Table S7. Three sediment isolates were not included in the consolidated bacterial phenotypic profile: E-MT10, for which no reliable Gram, KOH, or catalase information was obtained; D-MT04, which produced heterogeneous cellular material consistent with an unresolved or potentially mixed preparation; and D-MT08, for which bacterial cells could not be confidently visualized and which was therefore treated as a putative fungal morphotype for the purposes of post-cultivation characterization. These exclusions apply only to the isolate-level characterization layer; the corresponding colony morphotypes remain retained in the morphotype catalogue, crosswalk, and community matrix wherever applicable.

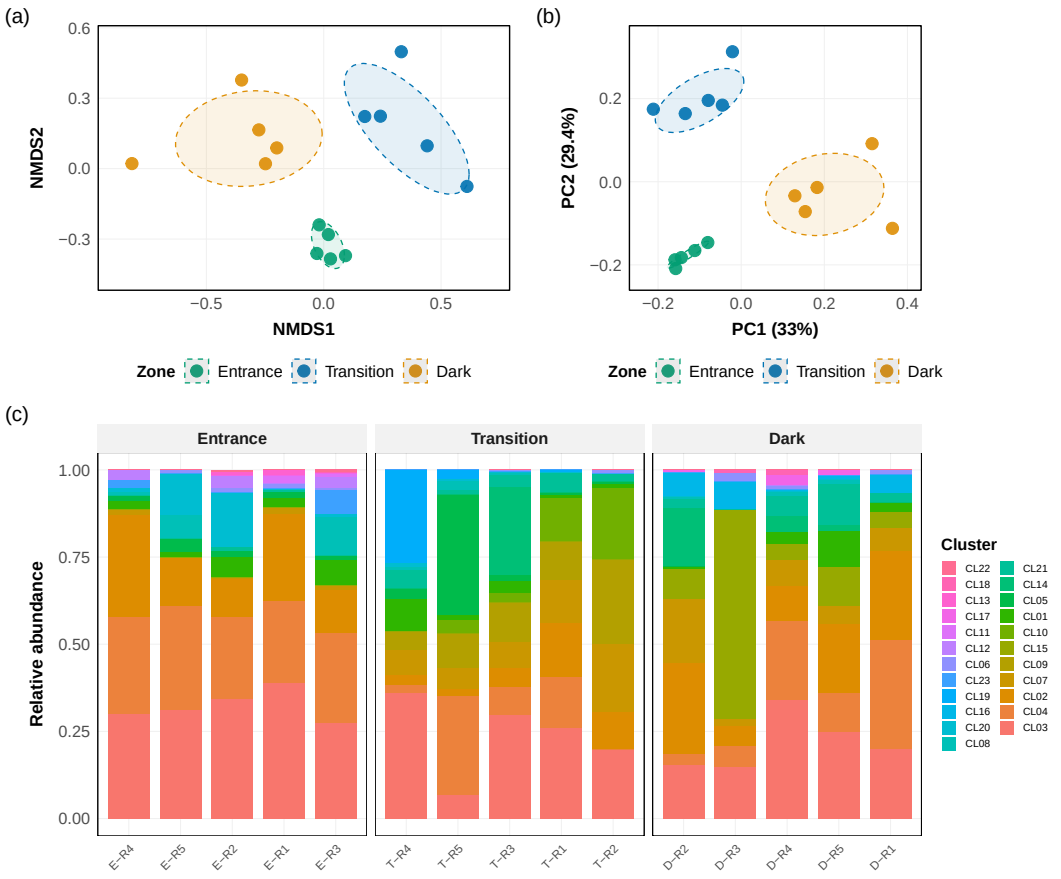

Figure 6. Compositional structure of the cultivable community in Experiment II (23-cluster crosswalk). **(a)** NMDS ordination of fifteen samples in phenotypic-cluster space using Hellinger-transformed abundances and Bray–Curtis dissimilarity (stress = 0.092). Points are colored by sector; ellipses represent 68% confidence regions around sector centroids. PERMANOVA: $R^2 = 0.573$, $F = 8.06$, $p = 0.001$; betadisper permutation $p = 0.334$. **(b)** PCoA ordination of the same dissimilarity matrix. **(c)** Relative abundance of the twenty-three operational phenotypic clusters per replicate, grouped by sector. Zone-restricted clusters are visually distinguished; the Transition sector carries three restricted clusters (CL09, CL10, CL19) at substantial collective abundance (~27% of the Transition community).

Among the isolates that yielded interpretable results across the characterization battery, rod-shaped or short rod-like cellular morphologies predominated across all three sectors. Cell dimensions ranged from small rod-shaped cells under approximately 1 µm (E-MT04, D-MT05) to larger rods exceeding 3 µm (E-MT08), with coccobacillus-like or short rod-like forms observed in E-MT01, E-MT09, T-MT01, T-MT07, D-MT01, and D-MT03. These shape descriptors are used here as conservative microscopic descriptions rather than taxonomic designations. Two isolates displayed cellular arrangements that may be useful for downstream taxonomic resolution: E-MT05, a Gram-positive coccus consistently observed in tetrads exceeding 1 µm in diameter, and D-MT06, a Gram-positive square rod-like cell type arranged in brick-like tetrads of approximately 1 µm per cell. Several isolates showed internal or staining features of potential interest under oil-immersion microscopy, including central refractile bodies in E-MT04, T-MT07, and one control isolate, and peripheral or surface-associated staining patterns in some mucoid isolates.

Gram staining and KOH string-test results showed a mixed pattern of concordance and discordance across the characterized isolate set. In this study, KOH string formation was

interpreted as compatible with a Gram-negative cell envelope, whereas absence of string formation was interpreted as compatible with a Gram-positive profile. Concordant cases were treated as higher-confidence assignments, whereas discordant cases were resolved by retaining the higher-confidence primary observation while preserving both raw outcomes in the detailed characterization record (Table S7). Several isolates produced tentative or low-confidence assignments, particularly among mucoid or slowly developing morphotypes, and three isolates were not assessable for consolidated bacterial characterization. For this reason, Gram results are interpreted as isolate-level descriptive information rather than as evidence for sector-level differences in cell-wall phenotype.

Catalase activity was detected in the majority of characterized isolates. A notable exception was the phenotypic cluster CL03 — the most abundant cluster in the dataset and a dominant or co-dominant morphotype in all three sectors. All three characterized members of CL03 (E-MT08, T-MT12, D-MT12) were catalase-negative, a shared phenotypic property that persisted across sectors despite Gram-level heterogeneity: E-MT08 was assigned as Gram-positive, whereas T-MT12 and D-MT12 were assigned as Gram-negative with lower confidence. Two additional cross-sector clusters showed Gram-level heterogeneity or uncertainty while maintaining catalase coherence. CL02 (E-MT02 G+; T-MT01 G^{-}; D-MT01 G+ tentative; all catalase-positive) combined high-confidence discordance between Entrance and Transition representatives with a tentative Dark-sector assignment. CL07 (E-MT09 G^{-} low-confidence; T-MT09 ambiguous/G^{-} retained cautiously; D-MT03 G+ tentative; all catalase-positive) should be interpreted more cautiously, because several assignments involve low-confidence or surface-associated staining features. In this cluster, the apparent Gram heterogeneity may reflect true cellular differences, culture-age effects, staining artifacts, or phenotypic convergence among colony-level morphotypes.

Within the Dark sector, the macroscopic mucoid morphotypes D-MT01 (CL02) and D-MT03 (CL07) produced visually convergent colony morphologies during subculture and partially similar microscopic and biochemical profiles, despite belonging to different phenotypic clusters in the primary colony-level crosswalk. This convergence does not indicate that the two morphotypes represent the same biological entity. Primary plate scoring assigned them as distinct units on the basis of colony-level traits observed during community scoring, and the community matrix preserves that assignment. Their later similarity during subculture is therefore interpreted as a characterization-level observation, potentially reflecting phenotypic plasticity, culture-age effects, or convergence among mucoid environmental isolates.

The characterization constrains the phenotypic possibilities of selected isolates and establishes a reference point for future molecular identification of the cryopreserved collection. The Gram-level heterogeneity and uncertainty observed within several cross-sector phenotypic clusters — especially CL02, CL03, and CL07 — indicate that the 23-cluster crosswalk can group cellularly distinct or ambiguously resolved organisms under shared colony-level phenotypic categories. This result does not invalidate the crosswalk, because the crosswalk was constructed from macroscopic colony traits before cellular characterization and was used only as an operational framework for community-level comparison. Rather, the characterization confirms

Table 5. Consolidated phenotypic characterization of sediment-derived representative isolates from Experiment II. Gram assignments summarize the final interpretation after repeat staining and KOH string-test comparison; raw test outcomes, confidence levels, and fresh cave-water control isolates are reported in Table S7. Tent.: tentative assignment; low conf.: low-confidence assignment. Shape descriptors are microscopic descriptions and should not be interpreted as taxonomic designations.

Code	Sector	Gram	Cell morphology	Catalase	Notes
E-MT01	E	G+ (tent.)	Coccobacillus-like, 1–2 µm	−	Faint staining
E-MT02	E	G+	Rod-shaped cells, 1.5–4 µm	+	CL02
E-MT04	E	G−	Small rod-shaped cells, <1–2 µm	+	CL05; refractile body
E-MT05	E	G+	Cocci in tetrads, >1 µm	+	CL04; diagnostic
E-MT07	E	G−	Slender rod-shaped cells, 2–3 µm	−	CL08
E-MT08	E	G+	Rod-shaped cells, >3 µm	−	CL03
E-MT09	E	G− (low conf.)	Rod-shaped to coccobacillus-like, variable	+	CL07; mucoid
T-MT01	T	G−	Very small rod-like/coccobacillus-like cells	+	CL02
T-MT02	T	G+	Rod-shaped cells	−	CL09; later successful stain
T-MT04	T	G+	Thick rod-shaped cells, 1–2 µm; chains	+	CL10; active division
T-MT07	T	G−	Coccobacillus-like cells, ~1 µm	+	CL05; refractile body
T-MT09	T	Ambig./G− retained	Rod-shaped to coccobacillus-like cells, 1.5–3 µm	+	CL07; peripheral staining
T-MT12	T	G−	Rod-shaped cells, 2–3 µm	−	CL03
D-MT01	D	G+ (tent.)	Rod-like to coccobacillus-like cells, 1–2 µm	+	CL02; peripheral staining
D-MT03	D	G+ (tent.)	Rod-like to coccobacillus-like cells, ~1 µm	+	CL07; mucoid
D-MT05	D	G−	Small rod-shaped cells, ~1 µm	−	CL04; revised stain
D-MT06	D	G+	Square rod-like cells, ≤1 µm; brick-like tetrads	+	CL15; diagnostic
D-MT12	D	G−	Rod-shaped cells, ~1 µm	−	CL03

that morphotype-cluster resolution is coarser than taxonomic or cellular resolution and that true biological diversity is necessarily underestimated by colony morphology alone.

A final case illustrates the separation between the morphotype-level community matrix and the later isolate-level characterization. CL06 was retained unchanged as a dark-centered pigmented phenotypic cluster in the cross-sector community matrix because its assignment was based on colony-level traits scored during the primary morphotype analysis. However, its Dark-sector representative, D-MT08, could not be characterized confidently as bacterial during Gram-stain review: bacterial cells were not reliably visualized, and an earlier fresh-culture preparation showed thread-like elements without diagnostic fungal structures. D-MT08 was therefore treated as a putative fungal morphotype in the characterization layer. This reassignment affects only the interpretation of the representative isolate and does not alter the original colony counts, the crosswalk, or any downstream community-level analysis.

4 Discussion

This study establishes, to my knowledge, the first spatially resolved cultivable baseline for an organal-type tropical volcaniclastic cave and shows that the light-defined zonation of the Organal San Antonio is associated with measurable differences in the R2A-recoverable microbial fraction. Three quantitative signatures were evaluated: cultivable density, local morphotype-cluster diversity, and morphotype-level community composition. The results converge on a specific and bounded interpretation: the aphotic interior supported lower cultivable density than the illuminated sectors, local morphotype-cluster richness and evenness showed no detectable sector-level differences, and community composition partitioned strongly with cave zonation. These patterns are consistent with environmental filtering across the entrance-to-interior gradient, but they do not isolate light as the sole causal driver. Rather, light-defined zonation in this cave integrates several covarying features — distance from the entrance, surface connectivity, sediment moisture, seepage, organic input, substrate heterogeneity, pH, and possibly mineral chemistry — that together define the ecological context in which the cultivable fraction was recovered.

Cultivable density followed a step-like pattern along the light-defined gradient rather than a graded linear decline. In Experiment II, the Entrance and Transition sectors supported statistically indistinguishable densities of approximately $5.1–5.6 \times 10^5$ CFU g^{-1} field-moist sediment, whereas the fully aphotic Dark sector supported approximately 8.9×10^4 CFU g^{-1} field-moist sediment, corresponding to an approximately sixfold reduction and a large sector effect ($\eta^2 = 0.652$). These values are based on aliquot-level gravimetric normalization using the estimated field-moist mass of the sediment aliquot used to prepare the mother suspension. This pattern was directionally consistent with Experiment I, where cultivable density was higher in illuminated than in aphotic sediments by a comparable margin, although the contrast did not resolve statistically at the available sample size (Hedges' $g = 1.16$; 95% CI crossing zero). The two experiments therefore support the same directional interpretation while differing in inferential strength: Experiment I

provides exploratory support, whereas Experiment II provides the primary three-sector test. Because Experiment I was incubated at approximately 20 °C under ambient laboratory conditions — the cave-mimetic cooling chamber was not yet available at that stage — absolute CFU values are not directly comparable between experiments; only the direction of the density contrast is informative across them.

The step-like density pattern is ecologically informative because the decline occurs only in the fully aphotic interior, while the Entrance and Transition sectors remain comparable in cultivable density. One plausible interpretation is that residual light, atmospheric coupling with the exterior, and seepage-mediated input in the illuminated and twilight sectors maintain a larger recoverable heterotrophic fraction than is supported in the deeper interior. This interpretation is consistent with the entrance-to-interior organization described in cave ecology [16, 17] and with the finding of Lavoie and colleagues that surface connectivity can be an important predictor of microbial community structure in lava caves [23]. However, the present study did not measure photosynthetically active radiation, dissolved organic carbon, sediment moisture, or geochemical input rates. The density contrast should therefore be interpreted as a sector-associated pattern within a light-defined cave gradient, not as direct evidence that light availability alone determines cultivable density.

Several features of the Organal San Antonio may have contributed to the magnitude of the density pattern. The geometry of an organal-type boulder-accumulation cave produces an abrupt transition from semi-illuminated to aphotic conditions, governed by the packing geometry of large volcaniclastic blocks rather than by gradual attenuation through a long open gallery. The distance between the Entrance and Transition sectors is approximately 30 m, and the Dark sector lies more than 80 m from the entrance, creating a compressed spatial gradient over which changes in light, airflow, seepage, and substrate conditions occur over short distances. The tropical montane context further maintains stable low temperatures and high relative humidity inside the cave, potentially reducing temporal noise and allowing spatial contrasts to be detected at small scales. At the same time, differences in sediment accumulation, organic matter retention, substrate surface area, and cave-water input among sectors remain unmeasured covariates. These factors could contribute to the observed density pattern independently of, or in interaction with, light-defined zonation.

The absence of detectable sector-level differences in local morphotype-cluster diversity is as important as the density pattern. In Experiment II, morphotype-cluster richness, Shannon diversity, and Simpson complement all remained statistically unresolved across sectors (all $p > 0.33$), and the same general pattern was observed in Experiment I. Together with the density result, this produces a specific dissociation: the Dark sector yielded fewer colonies per unit field-moist sediment, but not fewer local phenotypic clusters per replicate under the cultivation conditions used. The additional cultivable density recovered in the Entrance and Transition sectors was therefore not accompanied by a parallel increase in local morphotype-cluster richness or evenness.

This result should be interpreted at the correct biological resolution. Morphotype richness is not species richness, and the invariance reported here operates at the scale of colony-level phenotype, not at the scale of lineages, strains, or functional genes. Two isolates producing similar colony morphologies may belong to different species [46], while closely related organisms may generate distinguishable colony phenotypes under different physiological states or microenvironmental conditions [45]. What the data show is that sector identity did not detectably reduce the local number or evenness of operational colony phenotypes recovered on 25% R2A. Whether the same pattern holds at 16S rRNA gene, genome, or functional-gene resolution remains unresolved and will require molecular identification of the cryopreserved isolates and culture-independent profiling of the sediment community.

The strongest signal recovered by this study was the compositional partitioning of the cultivable fraction across the three sectors. PERMANOVA on the Hellinger-transformed 23-cluster matrix returned $R^2 = 0.573$ ($F = 8.06$, $p = 0.001$), with all pairwise contrasts significant after correction and with non-significant multivariate dispersion (betadisper permutation $p = 0.334$). The betadisper result is critical because it supports interpretation of the Experiment II PERMANOVA as sector-associated centroid separation rather than an artifact of unequal within-sector heterogeneity. This resolves the principal ambiguity of Experiment I, where PERMANOVA was significant but betadisper was also significant ($p = 0.021$), requiring conservative interpretation of the pilot compositional signal.

The compositional pattern had two components. First, seven cross-sector phenotypic clusters present in all three sediment sectors and treated as bacterial at the colony-catalogue stage (CL01–CL04, CL06–CL08) were detected throughout the cave, forming a shared cultivable core that persisted under the incubation conditions used. Several of these shared clusters changed quantitatively across the gradient; for example, CL03, the transparent punctiform cluster and the most abundant cluster overall, declined in mean count from Entrance to Transition to Dark. Second, this shared core was overlaid by zone-restricted phenotypic clusters. The Entrance sector contained four restricted clusters at low collective abundance; the Dark sector contained four restricted clusters contributing approximately 22% of its community; and the Transition sector contained three restricted clusters contributing approximately 27% of its community. The resulting pattern is not simply a loss of morphotypes with cave depth, but a reorganization of phenotypic-cluster composition across sectors.

The Transition sector is therefore not well described as a passive intermediate between Entrance and Dark. Three clusters restricted to the Transition sector (CL09, CL10, CL19) were recovered at substantial abundance and were absent from both adjacent sectors. This pattern suggests that the Transition sector may provide a distinct combination of conditions — strongly attenuated light, sustained humidity, seepage from the overlying substrate, and intermediate surface connectivity — that supports phenotypes not recovered elsewhere in the cave. This interpretation remains hypothetical because the study did not quantify nutrient concentrations, water chemistry, or light intensity at the replicate scale. CL09, in particular, should be interpreted cautiously because it carries low crosswalk confidence owing to phenotypic similarity with the

ubiquitous CL03; the ecological distinctiveness of the Transition sector rests more securely on CL10 and CL19, both assigned with higher confidence and together contributing approximately 24% of the Transition community. Molecular identification of the isolates corresponding to all three Transition-restricted clusters will be needed to determine whether they represent distinct biological entities or cases of morphotype convergence.

SIMPER results support this interpretation descriptively, but not inferentially. The Entrance–Dark contrast was driven primarily by quantitative reductions in shared clusters, especially CL03 and CL04, together with the contribution of the Dark-restricted CL15. The Transition–Dark contrast was driven by reciprocal replacement between the Dark-restricted CL15 and the Transition-restricted CL09. The Entrance–Transition contrast was dominated by abundance shifts in shared clusters, alongside contributions from Transition-associated CL09 and CL07. These patterns are useful for identifying which phenotypic clusters account for dissimilarity, but SIMPER does not test ecological mechanism. The stronger inferential result remains the combination of PERMANOVA, non-significant betadisper, and the observed distribution of shared and zone-restricted clusters.

The preliminary phenotypic characterization of representative isolates adds a cellular layer to the colony-level analysis. Rod-shaped or short rod-like morphologies predominated across sectors, with several distinctive cellular arrangements, including cocci in tetrads in E-MT05 and square rod-like cells in brick-like tetrads in D-MT06. Internal refractile structures observed in E-MT04, T-MT07, and one control isolate may provide useful constraints for future taxonomic identification, although they cannot be interpreted taxonomically without molecular or physiological confirmation. The characterization revealed Gram-level heterogeneity and uncertainty across several cross-sector clusters. CL03 contained a Gram-positive Entrance representative (E-MT08) and Gram-negative Transition and Dark representatives (T-MT12, D-MT12), with all three catalase-negative — a uniform feature that persisted across Gram-level heterogeneity. CL02 showed Gram heterogeneity among its characterized representatives, with a tentative Dark-sector reading. CL07 should be interpreted more cautiously: E-MT09 and T-MT09 were retained as low-confidence or ambiguous Gram assignments, and T-MT09 in particular showed peripheral purple staining with weak internal coloration, suggesting that culture age, staining artifacts, cell-surface properties, or physiological state may have contributed to the ambiguity. These observations were obtained from selected representatives rather than from all colonies within each cluster and should not be read as definitive cellular or taxonomic assignments. Instead, they constrain the phenotypic possibilities of the cryopreserved isolates and motivate molecular identification as the appropriate next step. These results show that the crosswalk can group cellularly distinct or ambiguously resolved organisms under shared colony-level phenotypic categories, confirming that the 23-cluster system is useful for community-level comparison but necessarily underestimates biological diversity.

This finding also justifies retaining the crosswalk as an operational phenotypic framework rather than retroactively splitting clusters after cellular characterization. The crosswalk was constructed from macroscopic colony traits observed during community scoring; Gram reaction,

KOH response, and catalase activity were measured later on selected isolates and at a different biological resolution. Restructuring the community matrix after observing partial cellular differences would risk introducing post hoc bias into the statistical analysis. The appropriate interpretation is therefore hierarchical: the crosswalk resolves morphotype-level community structure, while the characterization assays show that some morphotype clusters contain finer cellular heterogeneity that future molecular identification should evaluate.

The field observations provide ecological context for the cultivation data without serving as direct evidence for mechanism. Pigmented films near the entrance, translucent mucilaginous structures in the Transition sector, faint pale films in the Dark sector, visible seepage through the boulder matrix, and the detection of diatoms and ciliate protozoans in fresh sediment all indicate that the sampled substrate is part of a broader sediment-associated assemblage rather than an isolated bacterial layer. The presence of photosynthetic eukaryotes in Entrance-sector sediment is consistent with the visible phototrophic colonization of illuminated rock surfaces, while seepage in the Transition sector raises the possibility that dissolved organic matter transported from the surface contributes to the distinctive cultivable assemblage recovered there. Because this study did not measure dissolved organic carbon, nitrogen, phosphorus, or dripwater chemistry, this remains an ecological hypothesis rather than a demonstrated mechanism.

The pH measurements add an additional constraint on interpretation. Wet cave sediment was acidic (pH 4.40 in both a sediment–water preparation and a dense sediment preparation), whereas filtered cave stream water was less acidic (pH 5.74) and the diluted R2A medium was near neutral after autoclaving (pH 7.01). This contrast means that the recovered colonies represent organisms capable of forming colonies after transfer from acidic field-moist sediment to a low-nutrient, near-neutral cultivation medium. The culture-based dataset therefore should not be interpreted as a direct replica of the *in situ* community, but as the subset of organisms able to survive sampling, dilution, transfer, and growth under the imposed medium and incubation conditions. pH may be an important environmental filter in the cave, but the present design does not test pH effects directly; replicate-scale pH profiling of sediment and porewater would be a productive complement to future cultivation and molecular surveys.

The geological context of the Organal San Antonio adds a geomicrobiological dimension that remains largely unexplored. The cave occurs near the boundary between the Formación Combia and the Diorita de Támesis (Stock de Támesis), and the visible heterogeneity in rock texture, surface coloration, and mineral coatings suggests a complex substrate mosaic. Mineral composition could influence microbial colonization through trace-element availability, redox-active surfaces, pH microenvironments, adsorption of organic matter, or water-retention properties. None of these variables was quantified here. The present results therefore establish a biological baseline against which future geochemical and mineralogical analyses can be compared, rather than a mechanistic explanation of how substrate chemistry structures the cultivable community.

The inferential scope of this study is bounded by several methodological constraints. First, cultivation on dilute R2A recovers only a small fraction of total microbial cells in oligotrophic cave

sediments [37, 38]. The community structure documented here is the structure of the cultivable fraction under the specific conditions used: 25% R2A, aerobic incubation, low temperature, darkness, and Day-7 counting for the primary experiment. Whether the same spatial patterns occur in the uncultivated majority remains an empirical question. This limitation does not make cultivation uninformative: culture-based approaches recover viable organisms for downstream characterization and may access members of the rare biosphere or isolate-level diversity that are not fully resolved by molecular surveys alone [42]. Second, the study is spatial but not temporal. Both experiments sampled at single time points, so seasonal stability of the density and compositional patterns cannot yet be assessed. Third, the analysis concerns one cave. Generalization to other organales, volcaniclastic caves, or tropical pseudokarstic systems should be treated as a hypothesis for comparative work, not as a conclusion of this study.

Additional limits arise from analytical resolution and practical execution. Morphotype classification was performed by a single observer and was based on systematic visual criteria rather than independent inter-observer validation or algorithmic image clustering. The phenotypic crosswalk was constructed as a reproducible operational framework, but morphological convergence and phenotypic plasticity remain unavoidable sources of underestimation and uncertainty. Some low-confidence clusters, especially zone-restricted forms such as CL09, require molecular confirmation. Not all morphotypes recovered during primary plate scoring were photographed or purified with equal success during subsequent isolation steps, so the morphotype gallery should be read as representative rather than exhaustive; the complete analytical record is provided by the supplementary catalogues, crosswalk, and abundance matrices. Finally, the cooling chamber used for cave-mimetic incubation maintained the target temperature range with minor fluctuations, and the characterization battery was limited to Gram staining, KOH string testing, catalase assay, and light microscopy. These constraints define the resolution of the conclusions, but they do not erase the main patterns recovered: lower cultivable density in the aphotic sector, no detectable reduction in local morphotype-cluster diversity, and strong sector-associated compositional turnover with balanced multivariate dispersion.

Mucoid colony morphotypes are particularly susceptible to macroscopic convergence during subculture. In this study, the Dark-sector representatives of two different cross-sector mucoid clusters, D-MT01 in CL02 and D-MT03 in CL07, showed visually convergent colony morphologies and partially similar phenotypic profiles during characterization. This observation is treated as a characterization-level ambiguity rather than as evidence for merging the morphotypes: the crosswalk preserves the primary plate-scoring assignments without retroactive modification.

The Organal San Antonio is a tropical volcaniclastic cave whose cultivable microbial fraction is spatially structured across light-defined cave zonation. This study shows that cultivable density decreases in the aphotic sector, that local morphotype-cluster diversity remains statistically unresolved among sectors, and that phenotypic-cluster composition partitions strongly with cave zonation. The Transition sector emerged as a distinctive component of the system rather than a simple intermediate between Entrance and Dark, supporting zone-restricted phenotypes at substantial abundance. These findings establish a first quantitative cultivable baseline for an

organal-type pseudokarstic cave and provide a framework for future work. The next steps are clear: molecular identification of the cryopreserved isolates, culture-independent sequencing of sediment communities, replicate-scale physicochemical profiling, seasonal resampling, and comparative analysis across additional organales and volcaniclastic cave systems. This work does not claim to characterize tropical volcaniclastic cave microbiology as a whole; it defines one entrance into that uncharted category and establishes the empirical ground from which deeper biological and geomicrobiological questions can now be asked.

Data, Code, and Permits Availability

The R scripts, processed colony-count tables, morphotype matrices, crosswalk files, and supplementary analysis outputs associated with this thesis are available at `https://github.com/correa-gallego/psychro-oligophiles`.

Field collection and mobilization of biological material were conducted under the collection permit granted to Universidad EAFIT by the Autoridad Nacional de Licencias Ambientales (ANLA), Resolution No. 000548 of 28 March 2025.

References

1. Humboldt, A. V. & Bonpland, A. *Essai sur la géographie des plantes: accompagné d'un tableau physique des régions équinoxiales, fondé sur des mesures exécutées, depuis le dixième degré de latitude boréale jusqu'au dixième degré de latitude australe, pendant les années 1799, 1800, 1801, 1802 et 1803* DOI: 10.5962/bhl.title.9309 (Chez Levrault, Schoell et compagnie, libraires, Paris, 1805).

2. Nottingham, A. T. *et al.* Microbes follow Humboldt: temperature drives plant and soil microbial diversity patterns from the Amazon to the Andes. *Ecology* **99,** 2455–2466. DOI: 10.1002/ecy.2482 (2018).

3. Northup, D. E. & Lavoie, K. H. Geomicrobiology of Caves: A Review. *Geomicrobiology Journal* **18,** 199–222. DOI: 10.1080/01490450152467750 (2001).

4. Barton, H. A. & Northup, D. Geomicrobiology in Cave Environments: Past, Current, and Future Perspectives. *Journal of Cave and Karst Studies* **69,** 163–178 (2007).

5. Hershey, O. S. & Barton, H. A. in *Cave Ecology* (eds Moldovan, O. T., Kováč, Ľ. & Halse, S.) 69–90 (Springer International Publishing, Cham, 2018). DOI: 10.1007/978-3-319-98852-8_5.

6. Kováč, Ľ. in *Cave Ecology* (eds Moldovan, O. T., Kováč, Ľ. & Halse, S.) 297–307 (Springer International Publishing, Cham, 2018). DOI: 10.1007/978-3-319-98852-8_13.

7. Barton, H. & Jurado, V. What's Up Down There? Microbial Diversity in Caves. *Microbe* **2,** 132–138 (2007).

8. Oren, A. & Garrity, G. M. Valid publication of the names of forty-two phyla of prokaryotes. *International Journal of Systematic and Evolutionary Microbiology* **71,** 005056. doi: 10.1099/ijsem.0.005056 (2021).

9. Engel, A. S. in *Geomicrobiology: Molecular and Environmental Perspective* (eds Barton, L. L., Mandl, M. & Loy, A.) 219–238 (Springer Netherlands, Dordrecht, 2010). doi: 10.1007/978-90-481-9204-5_10.

10. Turrini, P., Chebbi, A., Riggio, F. P. & Visca, P. The geomicrobiology of limestone, sulfuric acid speleogenetic, and volcanic caves: basic concepts and future perspectives. *Frontiers in Microbiology* **15,** 1370520. doi: 10.3389/fmicb.2024.1370520 (2024).

11. Tomczyk-Żak, K. & Zielenkiewicz, U. Microbial Diversity in Caves. *Geomicrobiology Journal* **33,** 20–38. doi: 10.1080/01490451.2014.1003341 (2016).

12. Sarbu, S. M., Kane, T. C. & Kinkle, B. K. A Chemoautotrophically Based Cave Ecosystem. *Science* **272,** 1953–1955. doi: 10.1126/science.272.5270.1953 (1996).

13. Ortiz, M. *et al.* Making a living while starving in the dark: metagenomic insights into the energy dynamics of a carbonate cave. *The ISME Journal* **8,** 478–491. doi: 10.1038/ismej.2013.159 (2014).

14. Hoehler, T. M. & Jørgensen, B. B. Microbial life under extreme energy limitation. *Nature Reviews Microbiology* **11,** 83–94. doi: 10.1038/nrmicro2939 (2013).

15. Lever, M. A. *et al.* Life under extreme energy limitation: a synthesis of laboratory- and field-based investigations. *FEMS Microbiology Reviews* **39,** 688–728. doi: 10.1093/femsre/fuv020 (2015).

16. Howarth, F. G. Ecology of Cave Arthropods. *Annual Review of Entomology* **28,** 365–389. doi: 10.1146/annurev.en.28.010183.002053 (1983).

17. Culver, D. C. & Pipan, T. *The Biology of Caves and Other Subterranean Habitats* 2nd ed. (Oxford University Press, Oxford, New York, 2019).

18. Mulec, J. in *Cave Ecology* (eds Moldovan, O. T., Kováč, Ľ. & Halse, S.) 91–106 (Springer International Publishing, Cham, 2018). doi: 10.1007/978-3-319-98852-8_6.

19. Mulec, J., Kosi, G. & Vrhovsek, D. Characterization of Cave Aerophytic Algal Communities and Effects of Irradiance Levels on Production of Pigments. *Journal of Cave and Karst Studies* **70,** 3–12 (2008).

20. Zhu, H.-Z., Jiang, C.-Y. & Liu, S.-J. Microbial roles in cave biogeochemical cycling. *Frontiers in Microbiology* **13,** 950005. doi: 10.3389/fmicb.2022.950005 (2022).

21. Hathaway, J. J. M., Sinsabaugh, R. L., Dapkevicius, M. D. L. N. E. & Northup, D. E. Diversity of Ammonia Oxidation (amoA) and Nitrogen Fixation (nifH) Genes in Lava Caves of Terceira,

Azores, Portugal. *Geomicrobiology Journal* **31,** 221–235. DOI: 10.1080/01490451.2012.752424 (2014).

22. Kraft, N. J. B. *et al.* Community assembly, coexistence and the environmental filtering metaphor. *Functional Ecology* **29,** 592–599. DOI: 10.1111/1365-2435.12345 (2015).

23. Lavoie, K. H. *et al.* Comparison of bacterial communities from lava cave microbial mats to overlying surface soils from Lava Beds National Monument, USA. *PLOS ONE* **12,** e0169339. DOI: 10.1371/journal.pone.0169339 (2017).

24. Biagioli, F. *et al.* Outdoor climate drives diversity patterns of dominant microbial taxa in caves worldwide. *Science of The Total Environment* **906,** 167674. DOI: 10.1016/j.scitotenv.2023.167674 (2024).

25. Kosznik-Kwaśnicka, K., Golec, P., Jaroszewicz, W., Lubomska, D. & Piechowicz, L. Into the Unknown: Microbial Communities in Caves, Their Role, and Potential Use. *Microorganisms* **10,** 222. DOI: 10.3390/microorganisms10020222 (2022).

26. Zhu, H.-Z. *et al.* Bacteria and Metabolic Potential in Karst Caves Revealed by Intensive Bacterial Cultivation and Genome Assembly. *Applied and Environmental Microbiology* **87,** e02440–20. DOI: 10.1128/AEM.02440-20 (2021).

27. Northup, D. E. *et al.* Lava Cave Microbial Communities Within Mats and Secondary Mineral Deposits: Implications for Life Detection on Other Planets. *Astrobiology* **11,** 601–618. DOI: 10.1089/ast.2010.0562 (2011).

28. Halliday, W. R. Pseudokarst in the 21st Century. *Journal of Cave and Karst Studies* **69,** 103–113 (2007).

29. Northup, D. E. & Lavoie, K. H. in *Microbial Life of Cave Systems* (ed Summers Engel, A.) 161–192 (DE GRUYTER, 2015). DOI: 10.1515/9783110339888-010.

30. Hathaway, J. J. *et al.* Comparison of Bacterial Diversity in Azorean and Hawai'ian Lava Cave Microbial Mats. *Geomicrobiology Journal* **31,** 205–220. DOI: 10.1080/01490451.2013.777491 (2014).

31. Riquelme, C. *et al.* Actinobacterial Diversity in Volcanic Caves and Associated Geomicrobiological Interactions. *Frontiers in Microbiology* **6,** 1342. DOI: 10.3389/fmicb.2015.01342 (2015).

32. Nicolosi, G., Gonzalez-Pimentel, J. L., Piano, E., Isaia, M. & Miller, A. Z. First Insights into the Bacterial Diversity of Mount Etna Volcanic Caves. *Microbial Ecology* **86,** 1632–1645. DOI: 10.1007/s00248-023-02181-2 (2023).

33. Prescott, R. D. *et al.* Islands Within Islands: Bacterial Phylogenetic Structure and Consortia in Hawaiian Lava Caves and Fumaroles. *Frontiers in Microbiology* **13,** 934708. DOI: 10.3389/fmicb.2022.934708 (2022).

34. Gonzalez-Pimentel, J. L. *et al.* Prokaryotic communities from a lava tube cave in La Palma Island (Spain) are involved in the biogeochemical cycle of major elements. *PeerJ* **9,** e11386. DOI: 10.7717/peerj.11386 (2021).

35. De Waele, J., Sanna, L. & Rossi, A. *Pseudokarstic cavities in pyroclastic rocks: some examples from North Sardinia* in *Proceedings of the 10th international symposium on pseudokarst* (2008), 53–62.

36. Staley, J. T. & Konopka, A. Measurement of in situ activities of nonphotosynthetic microorganisms in aquatic and terrestrial habitats. *Annual Review of Microbiology* **39,** 321–346. DOI: 10.1146/annurev.mi.39.100185.001541 (1985).

37. Barton, H. Introduction to cave microbiology: A review for the non-specialist. *Journal of Cave and Karst Studies* **68,** 43–54 (2006).

38. *Cave Microbiomes: A Novel Resource for Drug Discovery* (ed Cheeptham, N.) DOI: 10.1007/978-1-4614-5206-5 (Springer New York, New York, NY, 2013).

39. Shu, W.-S. & Huang, L.-N. Microbial diversity in extreme environments. *Nature Reviews Microbiology* **20,** 219–235. DOI: 10.1038/s41579-021-00648-y (2022).

40. Amann, R. I., Ludwig, W. & Schleifer, K. H. Phylogenetic identification and in situ detection of individual microbial cells without cultivation. *Microbiological Reviews* **59,** 143–169. DOI: 10.1128/mr.59.1.143-169.1995 (1995).

41. Reasoner, D. J. & Geldreich, E. E. A new medium for the enumeration and subculture of bacteria from potable water. *Applied and Environmental Microbiology* **49,** 1–7. DOI: 10.1128/aem.49.1.1-7.1985 (1985).

42. Shade, A. *et al.* Culturing captures members of the soil rare biosphere. *Environmental Microbiology* **14,** 2247–2252. DOI: 10.1111/j.1462-2920.2012.02817.x (2012).

43. Kato, S. *et al.* Isolation of Previously Uncultured Slow-Growing Bacteria by Using a Simple Modification in the Preparation of Agar Media. *Applied and Environmental Microbiology* **84,** e00807–18. DOI: 10.1128/AEM.00807-18 (2018).

44. Yasir, M. Analysis of bacterial communities and characterization of antimicrobial strains from cave microbiota. *Brazilian Journal of Microbiology* **49,** 248–257. DOI: 10.1016/j.bjm.2017.08.005 (2018).

45. Haldeman, D. L. & Amy, P. S. Diversity within a Colony Morphotype: Implications for Ecological Research. *Applied and Environmental Microbiology* **59,** 933–935. DOI: 10.1128/aem.59.3.933-935.1993 (1993).

46. Lebaron, P., Ghiglione, J.-F., Fajon, C., Batailler, N. & Normand, P. Phenotypic and genetic diversity within a colony morphotype. *FEMS Microbiology Letters* **160,** 137–143. DOI: 10.1111/j.1574-6968.1998.tb12903.x (1998).

47. Cano Alzate, E. M. & Rentería Cárdenas, M. C. *Propuesta de clasificación de los organales en el Departamento de Antioquia, Colombia* Undergraduate thesis (Geology) (Universidad EAFIT, Medellín, Colombia, 2020).

48. Weber, M. *et al.* in *The Geology of Colombia, Volume 3: Paleogene–Neogene* (eds Gomez, J. & Mateus-Zabala, D.) 355–394 (Servicio Geológico Colombiano, Bogotá, 2020). DOI: 10.32685/pub.esp.37.2019.12.

49. Jaramillo, J. S., Cardona, A., Monsalve, G., Valencia, V. & León, S. Petrogenesis of the late Miocene Combia volcanic complex, northwestern Colombian Andes: Tectonic implication of short term and compositionally heterogeneous arc magmatism. *Lithos* **330-331,** 194–210. DOI: 10.1016/j.lithos.2019.02.017 (2019).

50. Servicio Geológico Colombiano. *Atlas geológico de Colombia 2023 a escala 1:500K* (Servicio Geológico Colombiano, Bogotá, Colombia, 2023).

51. González I., H. & Londoño, A. C. *Diorita de Támesis (Stock de Támesis) (k1dt), Cañón del Río Cauca, Departamento de Antioquia* (Instituto de Investigación e Información Geocientífica, Minero-Ambiental y Nuclear, INGEOMINAS, Bogotá, Colombia, 2002).

52. European Space Agency & Airbus. *Copernicus DEM* 2022. DOI: 10.5270/ESA-c5d3d65.

53. Patterson, T. & Kelso, N. V. *Natural Earth: Free vector and raster map data* 2023.

54. Instituto Geográfico Agustín Codazzi. *Límites municipales y departamentales de Colombia; cartografía hidrográfica local* Bogotá, Colombia, 2023.

55. D'Amico, S. *et al.* Psychrophilic microorganisms: challenges for life. *The EMBO Reports* **7,** 385–389. DOI: 10.1038/sj.embor.7400662 (2006).

56. Cavicchioli, R. On the concept of a psychrophile. *The ISME Journal* **10,** 793–795. DOI: 10.1038/ismej.2015.160 (2016).

57. Legendre, P. & Gallagher, E. D. Ecologically meaningful transformations for ordination of species data. *Oecologia* **129,** 271–280. DOI: 10.1007/s004420100716 (2001).

58. Anderson, M. J. Distance-Based Tests for Homogeneity of Multivariate Dispersions. *Biometrics* **62,** 245–253. DOI: 10.1111/j.1541-0420.2005.00440.x (2006).

59. Suslow, T. V. Application of a Rapid Method for Gram Differentiation of Plant Pathogenic and Saprophytic Bacteria Without Staining. *Phytopathology* **72,** 917–918. DOI: 10.1094/Phyto-72-917 (1982).

60. Oksanen, J. *et al. vegan: Community Ecology Package* 2026. DOI: 10.32614/CRAN.package.vegan.

61. Hsieh, T. C., Ma, K. H. & Chao, A. iNEXT: an R package for rarefaction and extrapolation of species diversity (Hill numbers). *Methods in Ecology and Evolution* **7** (ed McInerny, G.) 1451–1456. DOI: 10.1111/2041-210X.12613 (2016).

62. Ben-Shachar, M., Lüdecke, D. & Makowski, D. effectsize: Estimation of Effect Size Indices and Standardized Parameters. *Journal of Open Source Software* **5,** 2815. DOI: 10.21105/joss.02815 (2020).

63. Amrhein, V., Greenland, S. & McShane, B. Scientists rise up against statistical significance. *Nature* **567,** 305–307. DOI: 10.1038/d41586-019-00857-9 (2019).

64. Anderson, M. J. A new method for non-parametric multivariate analysis of variance. *Austral Ecology* **26,** 32–46. DOI: 10.1111/j.1442-9993.2001.01070.pp.x (2001).

Supplementary Material

This appendix provides the supplementary material supporting the sampling design, morphotype classification, cross-sector phenotypic crosswalk, isolate characterization, colony-count quality control, gravimetric normalization, rarefaction analysis, and exploratory pilot results. All morphotype clusters are operational phenotypic units and should not be interpreted as taxonomic assignments.

A. Sampling design schematic

Figure S1 summarizes the spatial structure of Experiment I and Experiment II along the cave gradient.

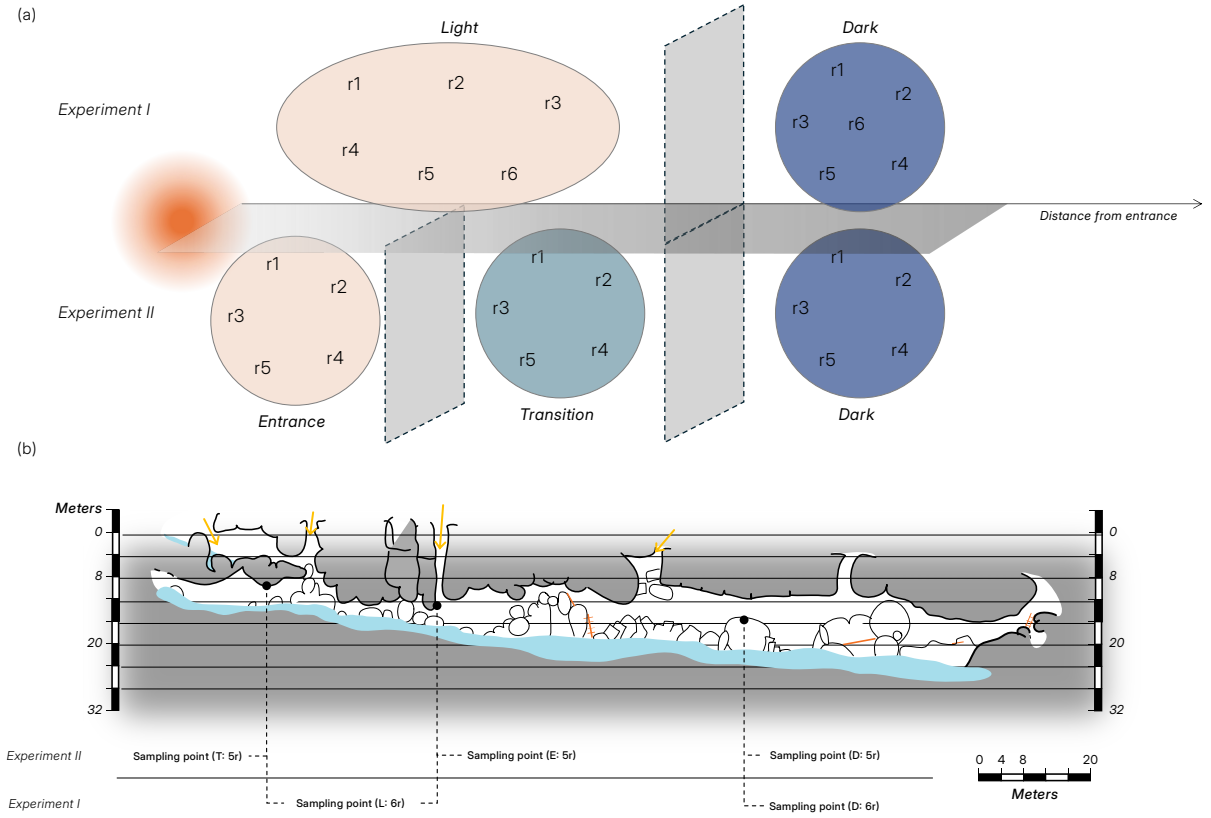

Figure S1. Sampling design and spatial layout of biological replicates in the Organal San Antonio. **(a)** Experimental structure along the cave's light-defined gradient. Experiment I compared Light and Dark categories with six biological replicates per category; Experiment II resolved the cave into Entrance, Transition, and Dark sectors with five biological replicates per sector. **(b)** Longitudinal cave cross-section showing the approximate position of sampling sectors, seepage points, and the cave stream. The schematic is spatially approximate and was adapted from the original cave survey by J. Rincón, R. Echeverri, A. Ledezma, and D. Estrada; Suunto and distance-meter survey, digitized by J. Rincón, 2–3 September 2017), modified by the author with permission.

B. Morphotype catalogue — Experiment I

Table S1 presents the nineteen morphotypes described during Experiment I. Fourteen codes were detected in countable plates and included in the community matrix; five appeared only in non-countable or excluded plates and are marked with an asterisk.

Table S1. Morphotype catalogue, Experiment I. Asterisk indicates morphotypes excluded from the Experiment I community matrix because they appeared only in non-countable or excluded plates.

Code	Color / Pigment	Shape / Elevation	Margin	Size (mm)	Texture / Surface	Transparency
ORG-SA001	Creamy white, variable	Circular to deformed, convex	Smooth to irregular	1–6	Firm, solid	Opaque
ORG-SA002	Cream, darker center	Filamentous, rhizoidal	Filamentous	15–40	Cottony, structured	Opaque
ORG-SA003	Viscous cream to pale yellow	Dome-like, irregular	Irregular	>10	Shiny, thick mucoid	Opaque
ORG-SA004	Transparent cream	Irregular smear, halo-like	Diffuse	3–4	Glossy, smooth	Translucent
ORG-SA005	Pale yellow-green	Irregular, flattened	Irregular	2–4	Thin mucoid veil	Translucent
ORG-SA006*	Pale pink, bluish edges	Circular, convex	Smooth	1–3	Glossy, gel-like	Semi-translucent
ORG-SA007	Purple central pigment	Circular, convex	Smooth	2–5	Soft, structured	Opaque
ORG-SA008	Yellow core, cream gradient	Circular, lobulate	Lobulate	2–6	Translucent, mucoid	Translucent
ORG-SA009	Creamy white, peripheral mucoid	Irregular, embedded in halo	Irregular	2–6	Wrinkled, complex	Opaque
ORG-SA010	Bright yellow, mucoid halo	Circular convex with mat	Lobulate, diffuse	3–8	Bright mucoid center	Translucent
ORG-SA011	White, slightly creamy	Circular to irregular, convex	Regular	2–5	Drop-like surface	Semi-translucent
ORG-SA012	White, embedded in mucoid mat	Convex circular in mat	Regular	1–4	Bright mucoid, microcolonies	Translucent
ORG-SA013*	Creamy, spectral yellow-green	Thin mat	Irregular	<1	Thin, nearly invisible	Semi-translucent
ORG-SA014*	Pale purple to white	Lobulate, slightly convex	Lobulate	2–4	Solid, dense	Opaque
ORG-SA015	Warm cream, shiny	Circular to irregular, convex	Smooth to undulate	2–5	Dense, firm	Opaque
ORG-SA016	Dark pink to burgundy	Circular, slightly convex	Slightly lobulate	2–4	Smooth, gel-like	Opaque
ORG-SA017*	Milky white	Convex, drop-like	Smooth	1.5–3	Smooth, clear	Semi-translucent
ORG-SA018*	White dense mat	Circular, embedded in mucoid	Diffuse	2–4	Opaque core, gelatinous ring	Opaque
ORG-SA019	Creamy yellow, granular halo	Circular, convex	Irregular	2–4	Slightly granular at margin	Opaque

C. Morphotype catalogues — Experiment II

Tables S2–S4 present the forty-two zone-specific sediment morphotype codes described during Experiment II: fifteen in Entrance, fourteen in Transition, and thirteen in Dark. Putative fungal morphotypes were identified conservatively from colonial macromorphology because lactophenol staining did not yield diagnostic fungal structures.

Table S2. Experiment II morphotype catalogue, Entrance sector. Fifteen morphotypes were described, including three putative fungal morphotypes.

Code	Color / Pigment	Shape / Elevation	Margin	Size (mm)	Texture / Surface	Transparency	Type
E-MT01	White-cream	Circular, convex	Entire	1–3	Smooth, glistening	Opaque	Bact.
E-MT02	Warm cream	Circular, convex	Entire	2–4	Smooth, glistening	Semi-translucent	Bact.
E-MT03	White-cream	Circular, umbonate	Entire	~2	Smooth, glistening	Opaque	Bact.
E-MT04	Yellow	Circular, elevated	Entire	~1	Smooth, glistening	Opaque	Bact.
E-MT05	White	Circular, convex, punctiform	Entire	0.5–1	Smooth, glistening	Opaque	Bact.
E-MT06	Dark purple-black center, pale cream margin	Irregular, elevated	Entire to slightly irregular	~1.5	Matte	Opaque	Bact.
E-MT07	Yellow with subtle green tint	Flat, spreading	Radial, lobulate	7–12	Glistening, spreading	Translucent	Bact.?
E-MT08	Near-transparent, faint cream	Circular, convex, punctiform	Entire	0.5–1	Smooth, glistening	Transparent to semi-translucent	Bact.
E-MT09	White-cream, mucoid appearance	Convex, irregular	Entire to deformed	6–8	Smooth, glistening, mucoid	Semi-translucent	Bact.
E-MT10	Bright yellow center with translucent halo	Umbonate center	Radial halo	2 center, up to 10 halo	Glistening	Opaque center, translucent halo	Bact.?
E-MT11	White-cream with faint pale pink tone	Circular, convex	Entire	1.5–4	Glistening, crystalline	Semi-translucent	Bact.
E-MT12	White to silver center with translucent halo	Circular, umbonate	Entire	1–2	Low luster	Opaque center, translucent halo	Bact.
E-MT13	White filaments	Flat, rhizoid	Rhizoid, irregular	~22 spread	Filamentous, glistening	Indeterminate	Fungal?
E-MT14	Pale cream, rhizoid, hyphal	Slightly elevated	Irregular, filamentous	10–25	Matte, fungal texture	Opaque	Fungal?
E-MT15	Very pale white	Flat, very large	Irregular, radial, asymmetric	40–50	Matte, thin growth	Opaque to thinly translucent	Fungal?

Table S3. Experiment II morphotype catalogue, Transition sector. Fourteen morphotypes were described, including two putative fungal morphotypes.

Code	Color / Pigment	Shape / Elevation	Margin	Size (mm)	Texture / Surface	Transparency	Type
T-MT01	Warm white-cream	Circular, convex	Entire	~6	Smooth, glistening	Mostly opaque	Bact.
T-MT02	Transparent, waterdrop	Circular, convex	Entire	0.5–1	Smooth, glistening	Transparent	Bact.
T-MT03	White	Punctiform, convex	Entire	~1	Smooth, glistening	Translucent	Bact.
T-MT04	Pale white center with clear halo	Circular, umbonate	Slightly irregular	2–3	Matte to smooth	Opaque center, clear halo	Bact.
T-MT05	Transparent	Punctiform, umbonate	Entire	~1	Smooth, glistening	Transparent	Bact.
T-MT06	Black center, cream border	Circular, umbonate	Subtly lobulate	~1	Not determined	Opaque	Bact.
T-MT07	Yellow	Circular, convex	Entire	~1	Smooth, glistening	Opaque	Bact.
T-MT08	White-cream	Circular, convex	Entire	~2.5	Smooth, glistening	Opaque	Bact.
T-MT09	Translucent, mucoid appearance	Circular, convex to irregular	Entire to irregular	~5	Smooth, glistening, mucoid	Semi-translucent	Bact.
T-MT10	Faint yellow-green center, thin mat	Flat, spreading	Entire to slightly irregular	~6	Smooth, glistening	Translucent	Bact.
T-MT11	Pale milky yellow	Circular, convex	Entire	~2	Smooth, glistening	Translucent	Bact.
T-MT12	Transparent	Circular, convex, punctiform	Entire	0.5–1	Glistening	Transparent	Bact.
T-MT13	White-warm cream, rhizoid, pubescent	Umbonate center, flat periphery	Poorly defined, rhizoid	7–9	Hairy, matte	Opaque	Fungal?
T-MT14	Pale cream, rhizoid, hyphal	Flat	Irregular, filamentous	~50	Matte, fungal texture	Thinly translucent	Fungal?

Table S4. Experiment II morphotype catalogue, Dark sector. Thirteen morphotypes were described, including one putative fungal morphotype.

Code	Color / Pigment	Shape / Elevation	Margin	Size (mm)	Texture / Surface	Transparency	Type
D-MT01	Translucent, milky cream	Circular, convex	Entire to slightly irregular	~3	Smooth, glistening	Semi-translucent	Bact.
D-MT02	White, firm	Circular, convex	Entire	2–3	Smooth, glistening	Opaque	Bact.
D-MT03	Transparent, highly mucoid appearance	Circular, convex, deformable	Entire to irregular	6–10	Smooth, glistening, mucoid	Translucent	Bact.
D-MT04	Pale milky yellow	Circular, convex	Irregular to entire	~3	Glistening, mucoid impression	Semi-translucent	Bact.
D-MT05	Warm white, punctiform	Circular, convex	Entire	~1	Glistening, firm, smooth	Opaque	Bact.
D-MT06	White-cream	Crateriform, slightly wrinkled	Diffuse, irregular	~1.5	Dry, matte	Opaque with faint halo	Bact.
D-MT07	White	Elevated, subtle central crater	Entire to subtly irregular	~2	Matte	Opaque	Bact.
D-MT08	Dark purple-black center with grey border	Flat to very low elevation	Entire, irregular	~2	Matte	Opaque	Bact.
D-MT09	Translucent yellow	Circular, convex	Entire	6–8	Translucent, mucoid	Translucent	Bact.
D-MT10	Pale translucent red-pink	Circular, convex, deformable	Entire to irregular	6–8	Translucent, mucoid	Translucent	Bact.
D-MT11	Faint spectral yellow	Flat, spreading	Radial, irregular	15–20	Glistening, irregular	Translucent	Bact.
D-MT12	Transparent	Circular, convex, punctiform	Entire	0.5–1	Smooth, glistening	Transparent	Bact.
D-MT13	White, pubescent	Elevated, convex, pubescent	Radial, regular	~12	Matte, hairy	Opaque	Fungal?

D. Cross-sector phenotypic crosswalk

Table S5 presents the final twenty-three-cluster crosswalk used to build the Experiment II community matrix. Assignments were based on macroscopic colony traits, and confidence levels indicate the strength of phenotypic matching. Fresh cave-water control morphotypes are shown only as environmental background correspondences and were not included in the sediment community matrix. Subsequent isolate-level characterization did not modify this crosswalk; D-MT08 remains in CL06 for community-matrix purposes, although it was later treated as not bacterial-assessable in the characterization layer.

Table S5. Cross-sector phenotypic crosswalk. Clusters are operational phenotypic units rather than taxonomic assignments. C-codes correspond to fresh cave-water environmental control morphotypes and were not included in the sediment community matrix.

Cluster	Cluster name	Conf.	Entrance	Transition	Dark	Water	Diagnostic features
CL01	Cream convex opaque	High	E-MT01	T-MT08	D-MT02	C-MT01	White-cream, circular convex, entire margin, opaque, smooth glistening, 1–4 mm
CL02	Warm cream translucent	High	E-MT02	T-MT01	D-MT01	—	Warm cream, circular convex, entire, semi-translucent with milky interior, smooth glistening, 3–6 mm
CL03	Transparent punctiform	High	E-MT08	T-MT12	D-MT12	—	Transparent to near-clear, circular convex punctiform, entire, smooth glistening, 0.5–1 mm, water-drop appearance
CL04	White punctiform	Moderate	E-MT05	T-MT03	D-MT05	C-MT05	White opaque, punctiform convex, entire, smooth glistening, 0.5–1 mm
CL05	Yellow small	High	E-MT04	T-MT07	—	C-MT02	Yellow, circular convex, entire, smooth glistening, opaque, approximately 1 mm
CL06	Dark-center pigmented	High	E-MT06	T-MT06	D-MT08	C-MT04	Dark purple-black center with pale or grey border, low elevation, matte, opaque, 1–2 mm
CL07	Mucoid large translucent	Moderate	E-MT09	T-MT09	D-MT03	—	Large, mucoid, translucent, irregular colony shape, convex to deformed, glistening, 5–10 mm
CL08	Spectral yellow-green mat	Moderate	E-MT07	T-MT10	D-MT11	C-MT03	Flat spreading, translucent yellow-green, radial or diffuse margin, uniform pigment, glistening, 7–20 mm
CL09	Transparent convex non-punctiform	Low	—	T-MT02	—	—	Transparent, circular convex, entire, smooth glistening, 0.5–1 mm; retained separately from CL03 because of non-punctiform appearance
CL10	Halo-bearing umbonate	Moderate	—	T-MT04	—	—	Pale white center with clear halo, umbonate, slightly irregular margin, matte, 2–3 mm
CL11	White umbonate	Low	E-MT03	—	—	—	White-cream, circular umbonate, entire, smooth glistening, approximately 2 mm, opaque
CL12	Pale pink/crystalline	Low	E-MT11	—	—	—	White-cream with faint pink tone, circular convex, semi-translucent crystalline, 1.5–4 mm
CL13	Silver-metallic halo	Low	E-MT12	—	—	—	White to silver center, translucent halo, umbonate, low luster, 1–2 mm
CL14	Milky yellow	Low	—	T-MT11	D-MT04	—	Pale milky yellow, circular convex, translucent to semi-translucent, approximately 2–3 mm
CL15	Crateriform matte	Low	—	—	D-MT06	—	White-cream, crateriform, slightly wrinkled, diffuse irregular margin, dry matte, approximately 1.5 mm
CL16	Central-crater white	Low	—	—	D-MT07	—	White, elevated with subtle central crater, entire to subtly irregular margin, matte, approximately 2 mm
CL17	Translucent yellow mucoid	Low	—	—	D-MT09	—	Translucent yellow, circular convex, mucoid, 6–8 mm
CL18	Red-pink translucent	Low	—	—	D-MT10	—	Pale translucent red-pink, circular convex, mucoid, liquid-like deformation, 6–8 mm
CL19	Transparent umbonate	Low	—	T-MT05	—	—	Transparent, punctiform umbonate with central tip, entire, smooth glistening, approximately 1 mm
CL20	Fungal rhizoid (Penicillium-like)	High	E-MT14	T-MT14	—	—	Pale cream, rhizoid with abundant hyphae, matte fungal texture, 10–50 mm
CL21	Fungal pubescent	Moderate	E-MT13	T-MT13	D-MT13	C-MT06	White, pubescent or hairy, elevated, matte opaque, radial margin, 10–22 mm
CL22	Fungal large asymmetric	Low	E-MT15	—	—	—	Very pale white, flat, very large, matte, asymmetric radial growth, 40–50 mm
CL23	Yellow-center halo	Low	E-MT10	—	—	—	Bright yellow umbonate center with translucent halo and pigment gradient, 2 mm center up to 10 mm halo

E. Fresh cave-water environmental control

Fresh, non-autoclaved cave stream water collected from the Dark sector was plated as an environmental water control. This control was distinct from the autoclaved cave stream water used as sterile diluent and was not included in the sediment community matrix.

Direct plating yielded 292 colonies from 100 µL, equivalent to 2.92×10^3 CFU mL^{-1}. Diluted plates yielded 21 colonies at 1:10 and 8 colonies at 1:100, equivalent to 2.10×10^3 and 8.00×10^3 CFU mL^{-1}, respectively. The 1:100 estimate should be interpreted cautiously because it derives from a low absolute colony count.

Table S6. Fresh cave-water environmental control morphotypes and colony counts. These morphotypes were recovered from non-autoclaved cave stream water and were not included in the sediment community matrix.

Code	Color / Pigment	Shape / Elevation	Margin	Size (mm)	Texture / Surface	Transparency	Type
C-MT01	White-cream	Circular, elevated	Entire, regular	3–4	Smooth, low luster	Opaque	Bact.
C-MT02	Yellow	Circular, convex	Entire, slightly diffuse	1–2	Smooth, glistening	Translucent	Bact.
C-MT03	Spectral yellow	Flat, spreading	Radial, diffuse	~10	Glistening, irregular	Translucent	Bact.
C-MT04	Purple-lilac	Circular, convex	Entire, regular	1–2	Matte, smooth	Opaque	Bact.
C-MT05	Pale cream, punctiform	Circular, convex	Entire, irregular	0.5–1	Low luster	Opaque	Bact.
C-MT06	White, pubescent	Convex, pubescent	Entire, radial	~10	Matte, hairy	Opaque	Fungal?

Fresh-water dilution	Colony count	CFU mL^{-1}
Undiluted	292	2.92×10^3
1:10	21	2.10×10^3
1:100	8	8.00×10^3

F. Detailed phenotypic characterization

Table S7 presents the per-test results for the representative isolates characterized in Experiment II. KOH string formation was interpreted as compatible with a Gram-negative cell envelope, whereas absence of string formation was interpreted as compatible with a Gram-positive profile. Isolates marked with † were excluded from the consolidated bacterial phenotypic profile because staining, purity, or bacterial cellular resolution could not be established. These exclusions do not modify the morphotype catalogue, cross-sector crosswalk, or community matrix.

Table S7. Per-test phenotypic characterization, Experiment II. Isolates marked with † were excluded from the consolidated bacterial phenotypic profile. KOH refers to the 3% KOH string test: "String" indicates viscous string formation, consistent with a Gram-negative cell envelope; "No string" indicates absence of string formation, consistent with a Gram-positive profile.

Code	Sect.	Gram	KOH	Conc.	Cat.	Conf.	Cell morphology	Notes
E-MT01	E	G+ tent.	String	D	−	M	Coccobacillus-like, 1–2 µm	Faint staining; Gram retained cautiously
E-MT02	E	G+	No string	Y	+	H	Rod-shaped cells, 1.5–4 µm	CL02 member; clear concordant result
E-MT04	E	G−	String	Y	+	H	Small rod-shaped cells, <1–2 µm	CL05 member; central refractile body
E-MT05	E	G+	No string	Y	+	H	Cocci in tetrads, >1 µm	CL04 member; diagnostic tetrad arrangement
E-MT07	E	G−	String	Y	−	H	Slender rod-shaped cells, 2–3 µm	CL08 member; clear concordant result
E-MT08	E	G+	No string	Y	−	H	Rod-shaped cells, >3 µm	CL03 member; catalase-negative
E-MT09	E	G− low conf.	No string	D	+	M/L	Rod-shaped to coccobacillus-like, variable	CL07 member; mucoid colony; Gram retained cautiously
E-MT10†	E	ND	ND	—	ND	—	Not determined	Yellow-center halo phenotype; excluded from consolidated bacterial profile
T-MT01	T	G−	No string	D	+	H	Very small rod-like/coccobacillus-like cells	CL02 member; repeated Gram result retained
T-MT02	T	G+	No string	Y	−	M	Rod-shaped cells	CL09 member; later successful stain; newly incorporated into consolidated profile
T-MT04	T	G+	No string	Y	+	H	Thick rod-shaped cells, 1–2 µm; chains	CL10 member; active division visible
T-MT07	T	G−	String	Y	+	H	Coccobacillus-like cells, ~1 µm	CL05 member; refractile body
T-MT09	T	Ambig./G− retained	No string	D	+	L	Rod-shaped to coccobacillus-like cells, 1.5–3 µm	CL07 member; mucoid colony; peripheral purple staining with weak internal coloration
T-MT12	T	G−	String	Y	−	H	Rod-shaped cells, 2–3 µm	CL03 member; catalase-negative
D-MT01	D	G+ tent.	No string	Y	+	M/H	Rod-like to coccobacillus-like cells, 1–2 µm	CL02 member; peripheral or surface-associated staining pattern
D-MT03	D	G+ tent.	No string	Y	+	M	Rod-like to coccobacillus-like cells, ~1 µm	CL07 member; concordant KOH result, but Gram assignment remains tentative due to peripheral/surface-associated staining
D-MT04†	D	ND	ND	—	ND	—	Heterogeneous cells	Probable mixed or unresolved preparation; excluded from consolidated bacterial profile
D-MT05	D	G− revised	No string	D	−	M/H	Small rod-shaped cells, ~1 µm	CL04 member; revised after repeat Gram staining; KOH discordant
D-MT06	D	G+	No string	Y	+	H	Square rod-like cells, ≤1 µm; tetrads	CL15 member; diagnostic brick-like arrangement
D-MT08†	D	ND / putative fungal	ND	—	ND	—	Not bacterial-assessable	CL06 representative in crosswalk; bacterial cells not confidently visualized; thread-like elements observed in earlier material
D-MT12	D	G−	String	Y	−	H	Rod-shaped cells, ~1 µm	CL03 member; catalase-negative
C-MT01	C	G−	String	Y	−	H	Coccobacillus-like cells, ~1 µm	Fresh cave-water control isolate
C-MT04	C	G−	No string	D	+	M/H	Rod-shaped cells, 1.5–2 µm	Fresh cave-water control isolate; Gram result retained

G. Colony counts and plate selection — Experiment II

Tables S8 and S9 present the Day 7 colony count and plate selection record for Experiment II. One primary plate per biological replicate was selected for density estimation by preferring countable plates with 30–300 colonies at the lowest dilution available. Technical replicate plates at 10^{-2} are indicated as T. TNTC indicates plates too numerous to count; NR indicates plates not recorded. Original total counts were retained as auditable records; morphotype-sum counts were used for downstream morphotype-based community analyses where discrepancies occurred.

Table S8. Colony counts and plate selection, Experiment II, Entrance and Transition sectors. This table forms the first part of the Experiment II plate-selection record; the Dark-sector record is provided in Table S9.

Plate ID	Zone	Rep.	Dilution	T	Count	Category	Selected
OSA-E1-D1	E	1	10^{-1}		—	TNTC	
OSA-E1-D2	E	1	10^{-2}		154	Countable	Yes
OSA-E1-D2b	E	1	10^{-2}	T	146	Countable	
OSA-E1-D3	E	1	10^{-3}		15	Low	
OSA-E2-D1	E	2	10^{-1}		—	TNTC	
OSA-E2-D2	E	2	10^{-2}		89	Countable	Yes
OSA-E2-D2b	E	2	10^{-2}	T	108	Countable	
OSA-E2-D3	E	2	10^{-3}		10	Low	
OSA-E3-D1	E	3	10^{-1}		—	TNTC	
OSA-E3-D2	E	3	10^{-2}		143	Countable	Yes
OSA-E3-D2b	E	3	10^{-2}	T	160	Countable	
OSA-E3-D3	E	3	10^{-3}		40	Countable	
OSA-E4-D1	E	4	10^{-1}		—	TNTC	
OSA-E4-D2	E	4	10^{-2}		167	Countable	Yes
OSA-E4-D2b	E	4	10^{-2}	T	—	TNTC	
OSA-E4-D3	E	4	10^{-3}		31	Countable	
OSA-E5-D1	E	5	10^{-1}		—	TNTC	
OSA-E5-D2	E	5	10^{-2}		76	Countable	Yes
OSA-E5-D2b	E	5	10^{-2}	T	109	Countable	
OSA-E5-D3	E	5	10^{-3}		13	Low	
OSA-T1-D1	T	1	10^{-1}		—	NR	
OSA-T1-D2	T	1	10^{-2}		163	Countable	Yes
OSA-T1-D2b	T	1	10^{-2}	T	130	Countable	
OSA-T1-D3	T	1	10^{-3}		21	Low	
OSA-T2-D1	T	2	10^{-1}		—	NR	
OSA-T2-D2	T	2	10^{-2}		194	Countable	Yes
OSA-T2-D2b	T	2	10^{-2}	T	125	Countable	
OSA-T2-D3	T	2	10^{-3}		11	Low	
OSA-T3-D1	T	3	10^{-1}		—	NR	
OSA-T3-D2	T	3	10^{-2}		137	Countable	Yes
OSA-T3-D2b	T	3	10^{-2}	T	123	Countable	
OSA-T3-D3	T	3	10^{-3}		11	Low	
OSA-T4-D1	T	4	10^{-1}		—	NR	
OSA-T4-D2	T	4	10^{-2}		33	Countable	Yes
OSA-T4-D2b	T	4	10^{-2}	T	56	Countable	
OSA-T4-D3	T	4	10^{-3}		7	Low	
OSA-T5-D1	T	5	10^{-1}		—	NR	
OSA-T5-D2	T	5	10^{-2}		94	Countable	Yes
OSA-T5-D2b	T	5	10^{-2}	T	101	Countable	
OSA-T5-D3	T	5	10^{-3}		5	Low	

Table S9. Colony counts and plate selection, Experiment II, Dark sector. This table forms the second part of the Experiment II plate-selection record; Entrance and Transition records are provided in Table S8.

Plate ID	Zone	Rep.	Dilution	T	Count	Category	Selected
OSA-D1-D1	D	1	10^{-1}		—	NR	
OSA-D1-D2	D	1	10^{-2}		95	Countable	Yes
OSA-D1-D2b	D	1	10^{-2}	T	105	Countable	
OSA-D1-D3	D	1	10^{-3}		10	Low	
OSA-D2-D1	D	2	10^{-1}		126	Countable	Yes
OSA-D2-D2	D	2	10^{-2}		10	Low	
OSA-D2-D2b	D	2	10^{-2}	T	14	Low	
OSA-D2-D3	D	2	10^{-3}		3	Low	
OSA-D3-D1	D	3	10^{-1}		152	Countable	Yes
OSA-D3-D2	D	3	10^{-2}		22	Low	
OSA-D3-D2b	D	3	10^{-2}	T	13	Low	
OSA-D3-D3	D	3	10^{-3}		2	Low	
OSA-D4-D1	D	4	10^{-1}		123	Countable	Yes
OSA-D4-D2	D	4	10^{-2}		31	Countable	
OSA-D4-D2b	D	4	10^{-2}	T	24	Low	
OSA-D4-D3	D	4	10^{-3}		2	Low	
OSA-D5-D1	D	5	10^{-1}		139	Countable	Yes
OSA-D5-D2	D	5	10^{-2}		23	Low	
OSA-D5-D2b	D	5	10^{-2}	T	31	Countable	
OSA-D5-D3	D	5	10^{-3}		0	Zero	

H. Gravimetric normalization — Experiment II

Table S10 presents the aliquot-level gravimetric normalization used for Experiment II density estimates. The mass represented in the mother suspension was estimated as $m_{\text{aliquot}} = m_{\text{tube}} \times 0.2/1.5$, where 0.2 mL was the sediment volume processed and 1.5 mL was the approximate field-moist sediment volume collected per tube.

I. Rarefaction analysis — Experiment II

Sample-size-based rarefaction and extrapolation curves for observed morphotype-cluster richness (Hill number $q = 0$) were computed with iNEXT using abundance data, 95% confidence intervals, and 200 bootstrap iterations. Rarefied richness at observed sample sizes corresponds to the observed counts reported in Table 3; extrapolated segments indicate expected richness at larger sampling effort. The curves indicate that morphotype-cluster richness was reasonably captured at the observed colony counts.

J. Statistical figures — Experiment I

Figures S3 and S4 present the graphical statistical output for Experiment I, which is retained as an exploratory binary Light–Dark comparison.

Table S10. Aliquot-level gravimetric normalization used for cultivable density estimates in Experiment II. m_{tube} is the measured field-moist sediment mass in each microtube. $m_{aliquot}$ is the estimated field-moist mass of the 200 µL sediment aliquot used to prepare the mother suspension.

Selected plate	Zone	Rep.	m_{tube} (g)	$m_{aliquot}$ (g)	Dilution	Count	$\log_{10}$(CFU g^{-1})
OSA-E1-D2	E	1	1.85	0.2467	10^{-2}	154	5.795
OSA-E2-D2	E	2	1.59	0.2120	10^{-2}	89	5.623
OSA-E3-D2	E	3	1.89	0.2520	10^{-2}	143	5.754
OSA-E4-D2	E	4	1.87	0.2493	10^{-2}	167	5.826
OSA-E5-D2	E	5	1.56	0.2080	10^{-2}	76	5.563
OSA-T1-D2	T	1	1.25	0.1667	10^{-2}	163	5.990
OSA-T2-D2	T	2	1.27	0.1693	10^{-2}	194	6.059
OSA-T3-D2	T	3	1.61	0.2147	10^{-2}	137	5.805
OSA-T4-D2	T	4	1.50	0.2000	10^{-2}	33	5.217
OSA-T5-D2	T	5	1.51	0.2013	10^{-2}	94	5.669
OSA-D1-D2	D	1	1.67	0.2227	10^{-2}	95	5.630
OSA-D2-D1	D	2	1.64	0.2187	10^{-1}	126	4.761
OSA-D3-D1	D	3	1.65	0.2200	10^{-1}	152	4.839
OSA-D4-D1	D	4	1.57	0.2093	10^{-1}	123	4.769
OSA-D5-D1	D	5	1.82	0.2427	10^{-1}	139	4.758

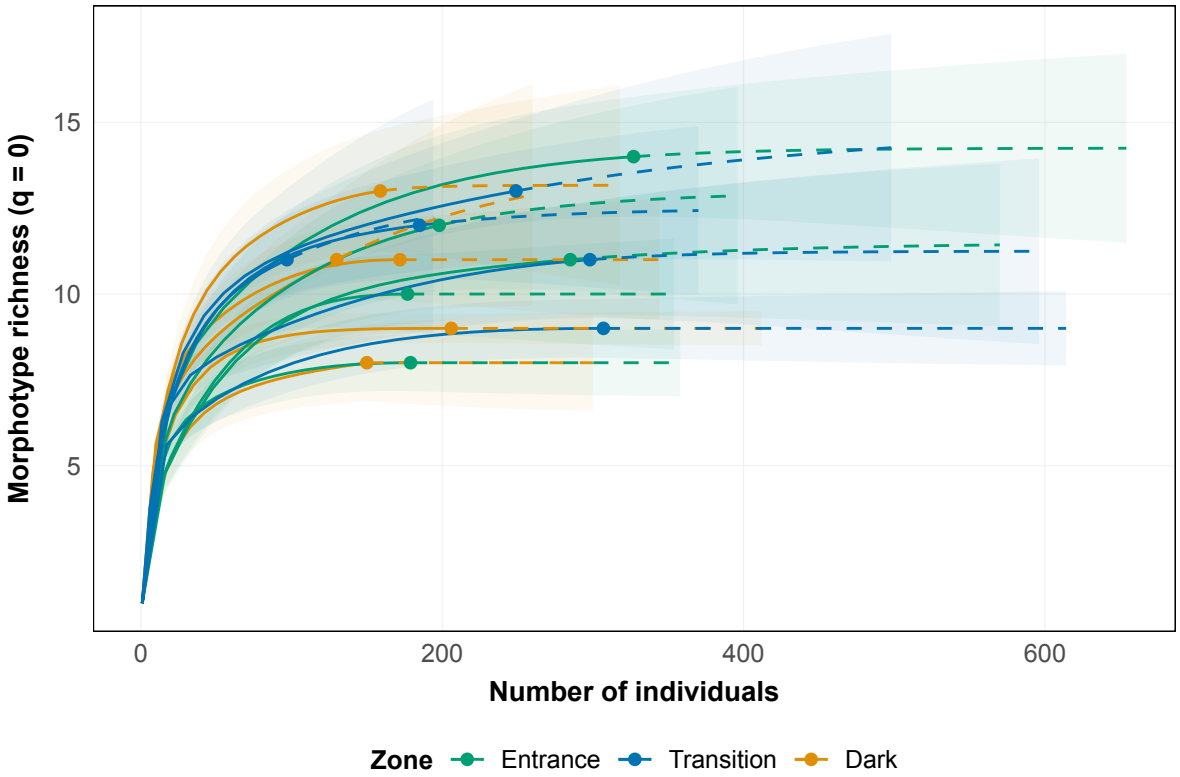

Figure S2. Sample-size-based rarefaction and extrapolation curves for morphotype-cluster richness (Hill number q = 0) across Experiment II sectors. Each curve corresponds to one biological replicate; points mark observed sample sizes and dashed segments represent extrapolation.

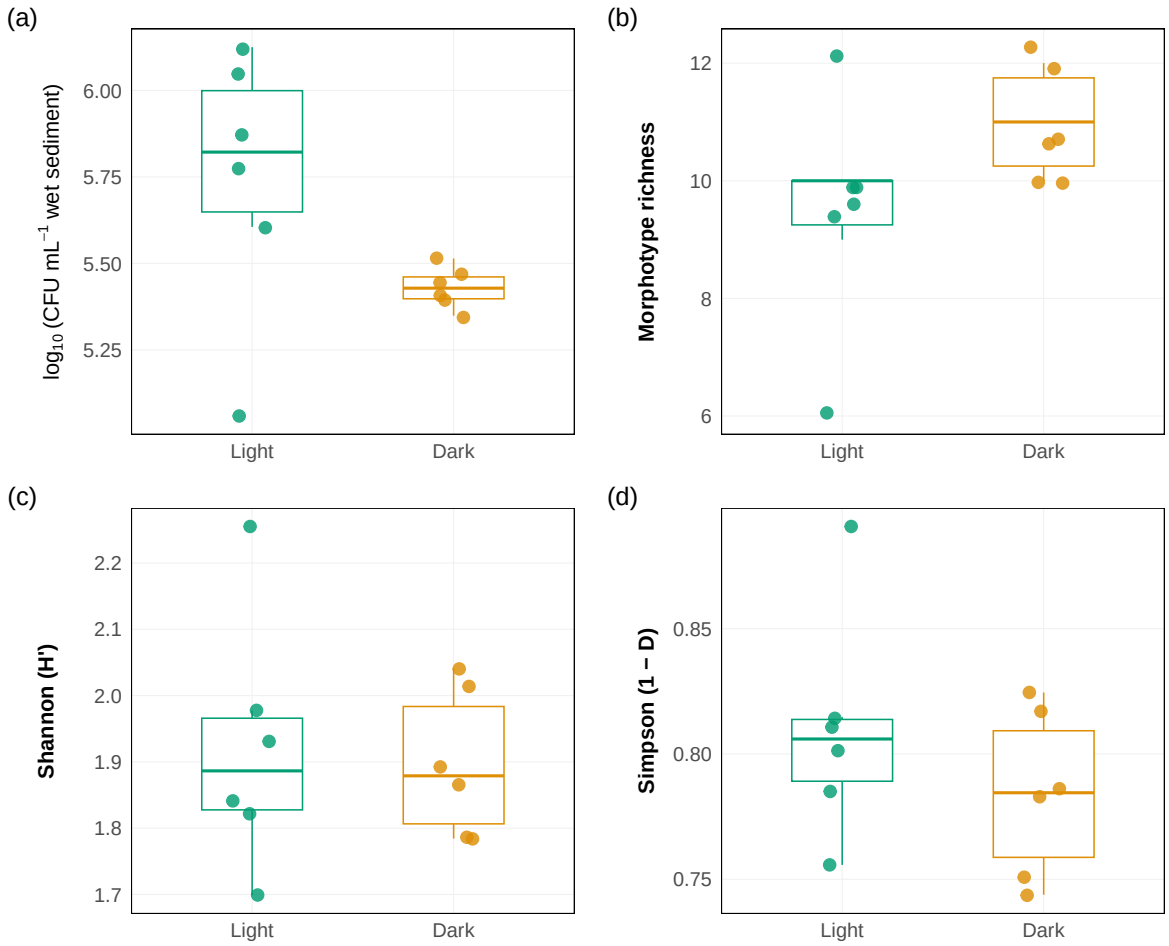

Figure S3. Cultivable density and local morphotype diversity, Experiment I. (a) $\log_{10}$(CFU mL^{-1} wet sediment) for Light and Dark categories. Wilcoxon rank-sum test: $W = 30$, $p = 0.066$; Welch t-test: $t = 2.015$, df = 5.2, $p = 0.098$; Hedges' $g = 1.16$, 95% CI −0.10 to 2.38. **(b–d)** Morphotype richness, Shannon diversity, and Simpson complement; no alpha-diversity metric showed a statistically resolved difference between categories.

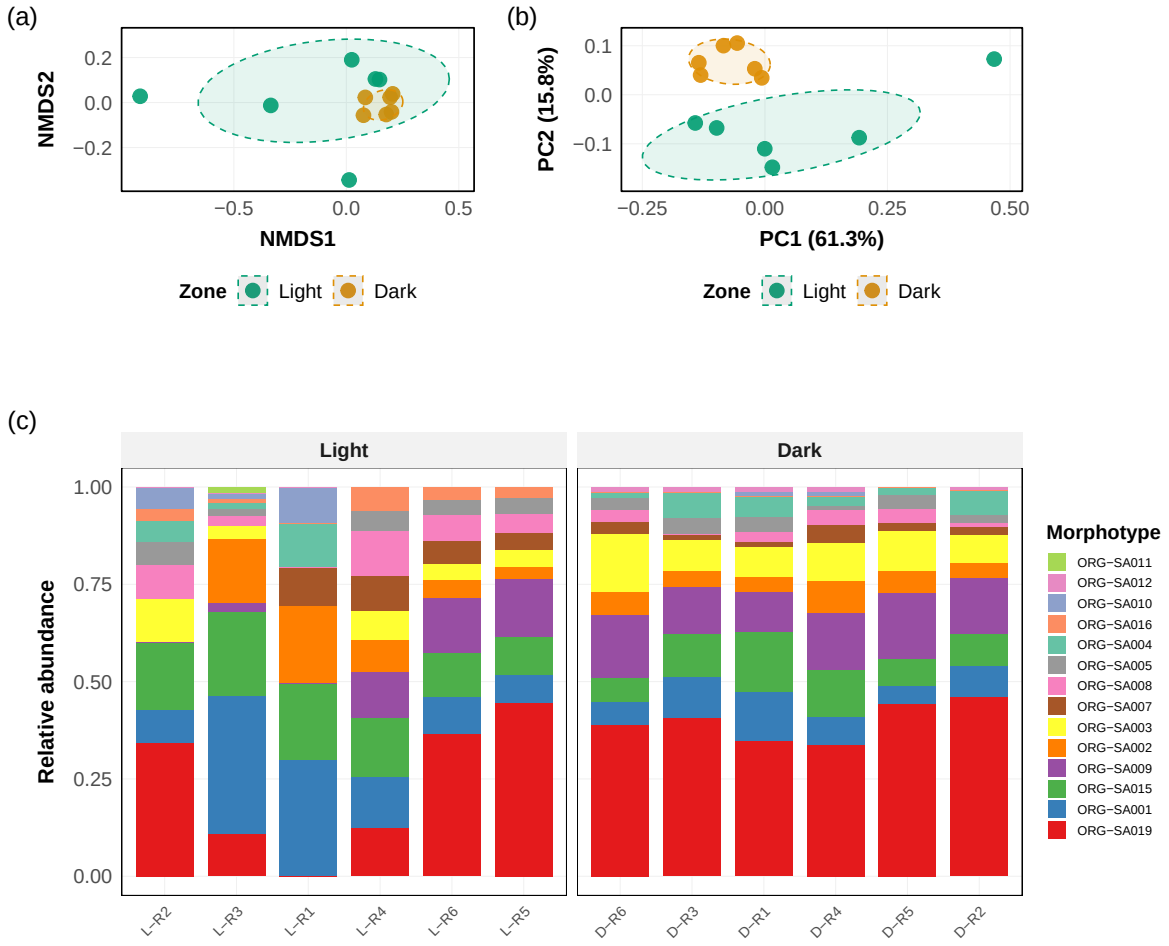

Figure S4. Compositional structure, Experiment I. (a) NMDS ordination using Hellinger-transformed abundances and Bray–Curtis dissimilarities. PERMANOVA: $R^2 = 0.227$, $F = 2.94$, $p = 0.021$; betadisper permutation test: $F = 5.39$, $p = 0.021$. Because dispersion differed between categories, this result is interpreted conservatively. **(b)** PCoA ordination. **(c)** Relative morphotype abundance per replicate.